Universität Potsdam

Leibniz-Institut für Astrophysik Potsdam (AIP)

master thesis

Analysis of the statistical properties of structures in the ISM using hydrodynamical simulations

Bogdan-Vasile Corobean

Advisor: Dr. Tobias Buck
First reviewer: Prof. Dr. Christoph Pfrommer
Second reviewer: Prof. Dr. Tim Dietrich

Potsdam, December 2021

Abstract

The interstellar medium (ISM) is a dilute, highly non-uniform medium, made up of gas, dust, magnetic fields, cosmic rays, and radiation. These components interact through physical processes on a wide range of spatial and density scales, which are currently unfeasible for cosmological simulations to resolve in a self-consistent manner. In this work we put forth a statistical model of the density structures in the ISM based on the analysis of results from the high resolution SILCC simulation. We first verify that the analysis is robust to changes in simulation resolution and, in preparation for future work, present a simple model for stellar winds using data from stellar evolution tracks. Next, starting from the widely accepted assumption than the interstellar gas follows a log-normal probability distribution function (PDF), we derive a model which relates the covering fraction, κ, (a measure the optical thickness of a spherical region) to the spatial scale of a region within the ISM, the volume-averaged density, and the clumping factor, C_ρ, (a measure of how structured a spherical region is). The model shows that κ evolves with density in a manner described by the error function (which is the cumulative of a log-normal PDF), however with a high degree of scatter which can be modelled using the clumping factor.

Contents

1 Introduction

The interstellar medium (ISM) is, alongside stars and stellar remnants, the most important visible component of a galaxy. It is a dilute, but highly non-uniform medium with densities ranging from less than 1, to a few hundred particles per cubic centimeter, consisting of atoms, ions (including cosmic rays), molecules, and dust. Radiation and magnetic fields are also ubiquitous.

An important feature of the ISM is that it is where star formation occurs. More precisely, this occurs in cold, dense structures called molecular clouds, which fragment, cool and collapse to form stars, binaries, and stellar clusters. The stars in turn influence molecular clouds through various so-called feedback mechanisms. UV radiation ionizes the surrounding gas and can dissociate molecules, while stellar winds and supernova explosions inject energy and momentum into the gas clouds and are also responsible for the chemical enrichment of the ISM. This complex interplay of physical processes on a wide range of scales is crucial for regulating star formation and, ultimately, galaxy evolution, however it is still not understood in a consistent way.

The goal of this project is to perform a statistical analysis of the density structures in the ISM with data from high-resolution numerical simulations. This work can potentially form the basis of a sub-grid model to be used in large scale simulations.

This thesis is structured as follows: Chapter 2 provides a brief review of the properties of the ISM and the most important physical processes that are at play there. In Chapter 3 we outline analysis methods used in this work, as well as the most important results. Finally, in Chapter 4 and Chapter 5 we summarize and discuss our findings.

2 Theoretical background

This chapter covers some basic aspects of the interstellar medium (ISM), in particular those which are relevant for the work presented here. We summarize the composition and phases of the ISM, the physical processes which are at play, turbulence and shocks. We also briefly describe molecular clouds and star formation, as well as the process which generates stellar winds.

2.1 The ISM

To better understand the ISM it is instructive to first go through its most basic components and outline the physical processes which determine the partition of the gas into its various *phases*.

2.1.1 The components of the ISM

The ISM is made up of gas (in neutral atomic, ionized and molecular form), dust, magnetic fields, cosmic rays, and radiation.

Gas Neutral hydrogen (HI) is the most abundant element in the ISM. While in this state, it is fairly easy to detect. Hydrogen atoms have a hyperfine transition from the interaction between the electron spin and the nuclear spin. The spin parallel state is characterized by a slightly higher energy than the spin antiparallel state. The neutral atoms are excited through collisions and the difference in energy between these energy levels have been very precisely measured in the laboratory to be 1420.4058 MHz (Hellwig et al., 1970), corresponding to a wavelength of 21.106 cm. The energy/temperature of this transition is very small ($\ll 1$ K), so it can be excited even in the coldest regions of the ISM. This so-called 21cm line is one of main tools for investigating the neutral gas in the galaxy, as well as at higher redshifts.

The ISM contains a significant amount of helium, $\sim 10\%$ by particle number (Williams, 2005). In addition to these elements, which are the products of Big Bang nucleosynthesis and are the most abundant in the ISM (as well as the Universe), other elements are created by stellar activity and released either via winds or supernova explosions: oxygen, carbon, nitrogen. There are also trace amounts of all the other elements, as well as a variety of molecules, which are found in cold, dense molecular clouds.

The temperature of the neutral gas in the ISM is $\sim$ 10K and the density is ~ 1 particle per cubic centimeter, however these properties can vary widely as a result of various physical processes acting on the gas, thus not all gas is neutral or in atomic form. The question of which are the stable states of the ISM gas

is a classic problem in astrophysics, one which has lead to the development of a theory of the ISM phases (see Section 2.1.2).

Dust About 1% of the mass of the ISM is in dust. It is formed in the atmospheres the outflows of stars and in supernovae, and is mainly made up of silicates and carbon (including polycyclic aromatic hydrocarbons, PAHs) (Draine, 2003).

The existence of dust can be inferred in a number of ways. First, since it emits at $\sim 20K$, its features can be detected in the infrared. Second, since it preferentially absorbs blue light, dust causes the reddening of background sources. The amount of reddening can be inferred by comparing stars of the same spectral type. Finally, dust causes *extinction*, i.e. a decrease in the observed brightness of an object due to the absorbtion and scattering of light along the way to the observer[1]. There are particular features of the extinction curve, most notably a "bump" at 217.5 nm associated graphite, which also point to the existence (Klessen & Glover, 2014).

Magnetic fields Magnetic fields have been detected in the ISM using various methods (Widrow, 2002): synchrotron emission (the emission of radiation in the radio part of the spectrum by a charged particle spiraling along magnetic fields), Faraday rotation (change in polarization of linearly polarized light as it passes through a medium in the presence of a magnetic field), Zeeman splitting (the splitting of a spectral line into several components in the presence of a magnetic field), and polarization of optical starlight (dust grains in the foreground absorb and re-emit polarized light). The average strength of the magnetic field is on the order of $\sim 1\mu$G, but can increase by an order of magnitude in HII regions and two orders of magnitude in molecular clouds and supernova remnants.

The origin of magnetic fields in the galaxy is unknown. However weak seed fields generated in the early Universe at cosmological phase transitions or through a Biermann battery process could then be amplified through a dynamo mechanism, such as differential rotation or small-scale velocity fluctuations (Widrow, 2002).

Magnetic fields are important for many processes in the ISM. They are essential in the mechanism of the magnetorotational instability (MRI) (Balbus & Hawley, 1991), which removes angular momentum in protostellar clouds thus playing

[1]Robert Trumpler is credited with the discovery of interstellar dust in 1930. He measured both angular diameter and photometric distances to 100 open star clusters, and found that there were differences between them. Angular diameter distances were found to be consistently smaller than expected when compared to the photometric distances, with the discrepancy increasing the farther away the clusters were. This suggested there was something along the line of sight, absorbing the light and making the objects appear dimmer, which Trumpler attributed to some "finely divided matter" (Trumpler, 1930).

a role in star and planet formation. Magnetohydrodynamic (MHD) turbulence is involved in cosmic ray acceleration (see Section 2.4), which then propagate propagate throughout the galaxy along magnetic field lines.

Since resistivity is negligible in the ISM, the ideal MHD approximation is valid in this case. This implies that magnetic fields are *frozen into the plasma*, i.e. the magnetic field moves with the gas.

Cosmic rays Cosmic rays (CRs) are highly energetic, relativistic charged particles (protons, electrons, and ions). In the Milky Way, they are approximately in equipartition with thermal and magnetic energy.

Cosmic rays do not interact with matter via scattering on individual particles, rather by scattering off electromagnetic waves or Alfvén waves. A remarkable characteristic of cosmic rays is that they follow a power-law distribution 33 orders of magnitude in flux and 12 orders of magnitude in energy (see Figure 1). This power law has two distinct features: a "knee" at 3×10^{15} eV, where the slope changes from -2.7 to -3.1, and an "ankle" at $\sim 10^{18}$ eV, where the slope hardens once again (Blasi, 2013).

The source of cosmic rays is still a topic of research. A potential clue can be found the *Hillas criterion* (Hillas, 1984), which provides an energy limit for CRs depending on the size of the source

$$\mathrm{E_{max}} = \mathrm{Ze}\beta\mathrm{BR} \tag{1}$$

which relates the maximum energy of a particle to the ion charge Ze, the magnetic field B, the characteristic velocity of scattering centers $\beta = u/c$, and the characteristic scale of the shock R. According to this, the Larmor radius of the particle being accelerated cannot exceed the size of the source, suggesting that the highest energy cosmic rays, in particular those beyond the knee, most likely come from outside the galaxy. Galactic sources include pulsars, type II supernovae, and shocks from supernova remnants and stellar winds, while extragalactic sources include gamma ray bursts and active galactic nuclei (AGN). Since cosmic rays move along magnetic fields lines in the galaxy, it is impossible to trace a particle to its exact source. Instead cosmic ray sources can be determined via the detection of gamma rays, which are by-products of cosmic ray interactions.

The process which accelerates cosmic rays is a classic problem in astrophysics. Enrico Fermi proposed a mechanism in which charged particles interact with the moving irregularities in the magnetic fields which are found throughout interstellar space (Fermi, 1949). Particles gain energy with each reflection off these "magnetic mirrors" and if they remain in this region for some characteristic time τ a power-law distribution of particle energies is obtained, matching the observation. In the following decades the basic Fermi acceleration mechanism has been

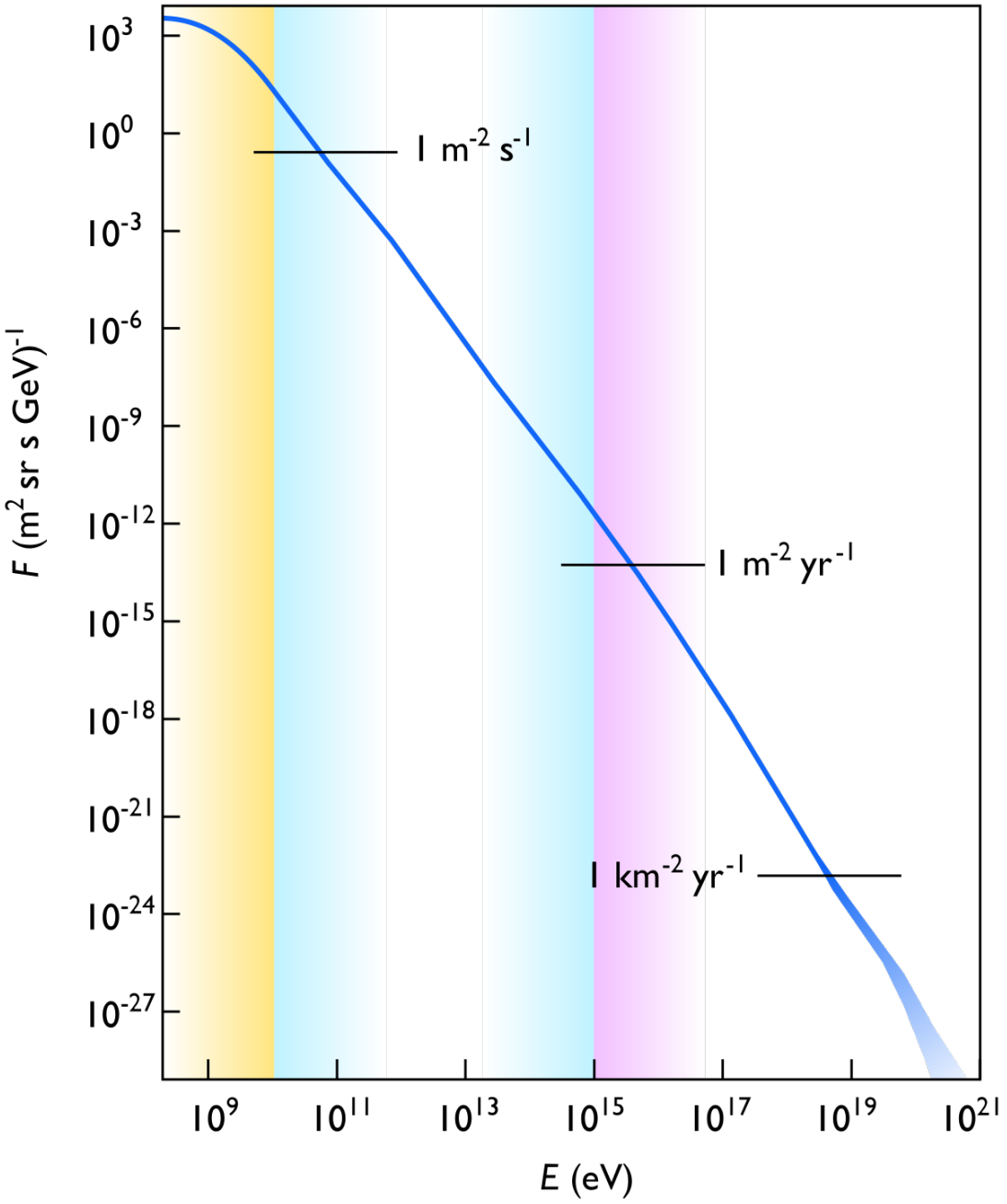

Figure 1: Cosmic ray flux as a function of cosmic ray energy. On a logarithmic scale the relation is linear with a slope of -2.7. The plot has two main features: a "knee" at 3×10^{15} eV, where the slope becomes -3.1, and an "ankle" at $\sim 10^{18}$ eV, where the slope reverts to its original value. CRs beyond the knee are thought to be energetic enough that they must originate from outside the galaxy. Image source: Wikimedia Commons.

refined and put on solid theoretical grounds and is currently the most successful theory of cosmic ray acceleration (see Section 2.4 for details).

Radiation The properties of the ISM are determined in large part by the interaction of the gas and dust with the interstellar radiation field (ISRF). The energy density of the ISRF consists of the following components:

- galactic synchrotron (radio) emission from relativistic electrons
- the CMB
- infrared and far-infrared emission from dust grains heated by starlight
- bound-bound, bound-free, and free-free emission from 10^4 K ionized plasma
- X-rays from $10^5 - 10^8$ K plasma

In the ISM, most of the energy density is in the infrared (thermal dust emission and CMB) and in the optical and UV (starlight) (Klessen & Glover, 2014).

2.1.2 Phases of the ISM

With regards to its thermal and chemical properties, the ISM can be divided into a series of *phases*. According to an influential early model presented by Field, Goldsmith and Habing in 1969 (Field et al., 1969), atomic gas in thermal equilibrium in the ISM can exist in two states: cold, dense gas with T $\sim$ 100 K (according to modern nomenclature, this is the *cold neutral medium*, CNM) and warm, diffuse gas with T $\sim 10^4$ K (the *warm neutral medium*, WNM). Gas at intermediate temperatures is thermally unstable, so it would either cool and increase in density, or heat up and decrease in density. This model was extended by McKee & Ostriker (1977), who posited that gas in the ISM would be heated by supernovae, creating large ionized bubbles filled with hot gas with T $\sim 10^6$ K (*hot ionized medium*, HIM). While this gas is expected to cool, the cooling time at T $\sim 10^6$ K is significantly larger than the cooling time in the range 10^4 to 10^6 K, so most of the gas will be found at about 10^6 K (Klessen & Glover, 2014).

Even before these models were being put forth, there was observational evidence of an extensive layer of warm (10^4 K), low density (10^{-1} cm$^-$1) gas surrounding the plane of our galaxy, which has been ionized by young, massive type O stars (Hoyle & Ellis, 1963). Further observations confirmed the existence of what is now known as the *warm ionized medium* (WIM) (Haffner et al., 2009), which contains about 90% of the ionized gas in the ISM. The current picture of the ISM is that it contains clumps of CNM gas, surrounded by the increasingly

	MM	CNM	WNM	WIM	HIM
n [cm^{-3}]	10^2 - 10^5	4...80	0.1...0.6	0.2	10^{-3} .. 10^{-2}
T [K]	10-50	50-200	5500 - 8500	8000	10^5 - 10^7
f_{vol}	< 0.01	$0.02 - 0.04$	0.3	0.2	0.5
f_{mass}	0.2	0.4	0.3	0.1	0.01

Table 1: A summary of the properties of the different phases of the ISM.

hot and tenuous WNM and WIM, and finally the HIM, which fills most of the volume.

In addition to the atomic gas in its various phases, the ISM also contains cold, dense molecular clouds. Molecular gas plays an important role in star formation.

For many practical purposes, the gas in the ISM can be treated as two phases in equilibrium: the CNM and the WNM (Field et al., 1969; Wolfire et al., 2003). This can be explained by considering the heating and cooling processes in the ISM (Bialy & Sternberg, 2019) (for more details see Section 2.1.3).

2.1.3 Physical processes in the ISM

As previously mentioned, heating and cooling processes are crucial for explaining the structure and properties of the ISM. The division into the CNM and WIM can be explained theoretically just by considering these processes (Field et al., 1969).

Heating mechanisms

- photoelectric heating
- X-ray and cosmic ray heating
- H_2 heating
- cosmic rays
- PdV work and shock heating from stellar winds, supernovae

Photoelectric heating occurs when far UV (FUV) photons collide with dust and PAHs in the ISM releasing energetic electrons which then thermalize with the gas. The energy of this electron is equal to the difference between the energy of the photon and the energy barrier that needs to be overcome in order to detach the electron from the grain, which can be on the order of an eV (Klessen & Glover, 2014). A similar process can also happen with more energetic X-ray photons or cosmic rays, which ionize atoms or molecules, with the resulting electrons adding

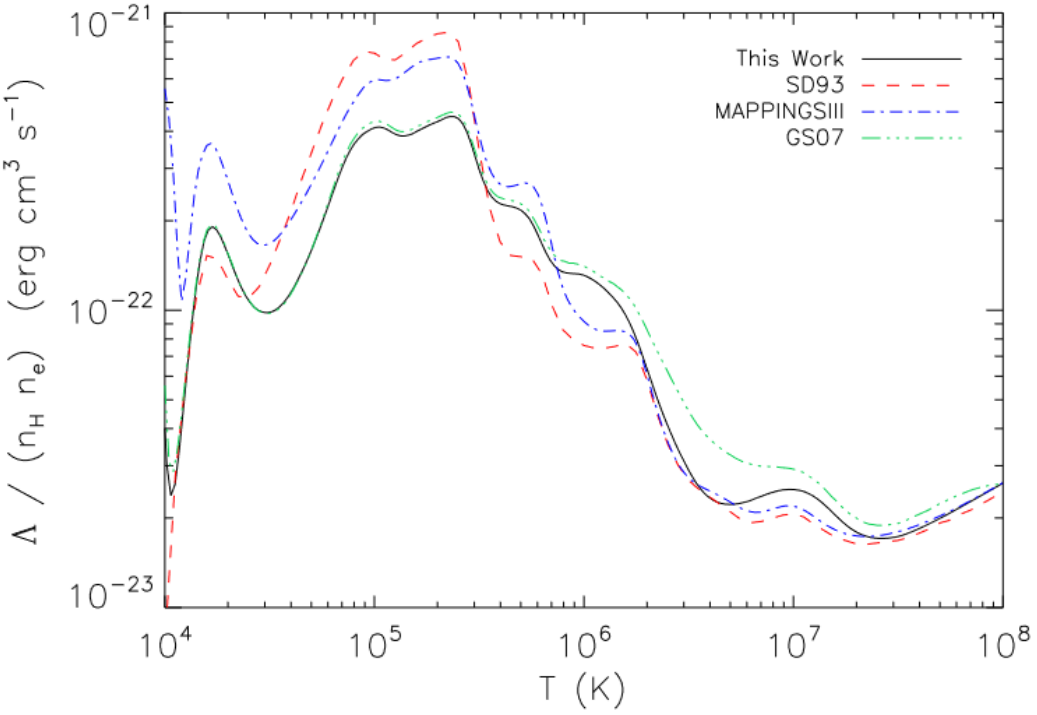

Figure 2: Comparison between normalized cooling rates for a plasma in collisional ionization equilibrium (CIE) from studies using different versions of the `CLOUDY` and `MAPPINGS` codes. While there are slight differences in the cooling functions, all find the highest cooling rates at about 10^5 K (see Wiersma et al., 2009, for details)

their energy to the gas. Cosmic rays are particularly important in gas that is shielded from the interstellar radiation field (ISRF).

Another important heating mechanism is via kinematic effects: PdV work and shock heating from supernovae. As supernovae explode, they inject a significant amount of energy into the ISM, roughly 10^{51} ergs per event. Massive stars release comparable amounts of energy throughout their lifetimes as stellar winds. In fact the existence of the hot phase of the ISM was first proposed to be a result of supernova explosions (McKee & Ostriker, 1977).

Cooling mechanisms

- Lyα cooling
- fine structure cooling (CII, OI atoms)

- H_2 cooling

In this case, the fundamental process is a collisional excitation followed by radiative decay. Lyα cooling occurs as a result of electron impact, while fine structure line emissions are excited primarily collisions with the neutral hydrogen atoms (Wolfire et al., 2003; Bialy & Sternberg, 2019).

Lyα cooling takes place at large temperatures($\sim 10^4$ K). Below this temperature, cooling via fine structure transitions (of mainly CII and OI atoms) plays an important role. Finally, there is H_2 cooling via rotational and vibrational transitions, which is significant at higher temperatures (above $\sim$ 500K, the first accessible rotational transition of the H_2 molecule), however it is very inefficient at lower temperatures (Klessen & Glover, 2014). In the warm, diffuse ISM, H_2 cooling can be dominant at low metallicities and high ISFR strength (Glover & Clark, 2014).

Cooling processes in the ISM are usually described by a cooling function $\Lambda(T)$, which is given in units of energy emitted/volume/time. An example of this is shown in Figure 2, which illustrates the cooling rate of a plasma at different temperatures. Note that cooling is also a function of metallicity, so different cooling functions must be computed for different environments and must take into account chemical enrichment if that is a factor.

It is also relevant to note that, since at low densities cooling is a collisional process involving two particles (Wiersma et al., 2009), cooling functions are often given in terms of n^2 (where n is the particle density) when describing a fully ionized plasma, or as a product between the particle densities of different species if they are not assumed equal (e.g. hydrogen atoms and electrons). The heating rate however, a process which usually involves a particle and photons or cosmic rays, scales with n.

2.2 The SILCC simulation

The ISM is a multiphase system, consisting of cold, warm, and hot gas, in atomic, ionized or molecular form, influenced by a complex set of physical processes (heating, cooling, chemical enrichment). These processes act on a wide range of scales, from the typical size of a molecular cloud ($\sim$ 50 pc), to the size of protostellar disks ($\sim$ 100 AU), while outflows launched by supernovae can escape beyond the galactic disk at scales of $\sim$ kpc. Cold, molecular gas may collapse to form massive stars, which in turn have a significant effect on the ISM through feedback processes: radiation, stellar winds, supernova explosions. The SILCC project[2] (*SImulating the Life-Cycle of molecular Clouds*, Walch et al., 2015; Girichidis et al., 2016) is a series of state-of-the-art numerical simulations of the gas in the

[2]http://silcc.mpa-garching.mpg.de/

ISM with the aim of understanding the life cycle of molecular self-consistently, taking into account all the processes and the scales involved.

In order the model the ISM, the simulation was performed using the fully 3D `FLASH 4.1` MHD code with AMR (adaptive mesh-refinement), which allows to resolve in high-resolution, high-density regions, meaning a wide range of density scales can be accurately characterized. The setup is a $(500\ \mathrm{pc})^2 \pm 5$ kpc "tall box" corresponding to a segment of a typical galactic disk at low redshift with solar neighborhood properties. In order to obtain an accurate picture of the ISM, the simulation includes:

- an external galactic potential
- self-gravity
- radiative heating and cooling
- chemical evolution (which follows the formation of H_2 and CO molecules)
- feedback from supernova explosions

Several simulation runs are available with resolutions ranging from 4 pc to 0.5 pc, significantly higher than what can be achieved with cosmological simulations[3]. Recent projects such as EAGLE (Schaye et al., 2015) and IllustrisTNG (Pillepich et al., 2018) thus need to employ sub-grid models for physical processes which occur on smaller scales. Due to its high resolution, the SILCC simulation is particularly suited for the purposes of this analysis (see Chapter 3), as it includes a self-consistent treatment of many physical processes that are relevant for the ISM.

2.2.1 Stellar feedback

Simulations of the ISM have shown that stellar feedback also plays an important role in the gas phase distribution. In particular, as we have seen, the WNM/WIM are heated by supernova explosions, so the position of supernovae within the medium is one of the factors which affects the ISM phase distribution. To illustrate this point, we briefly go through some results of the SILCC simulation (Walch et al., 2015), since it was also used for the analysis presented in this work.

One approach is to have supernovae explode in the densest regions. Star clusters form where there is an abundance of gas and it is reasonable to assume that there will be more supernova explosions where there are more stars (this

[3]For a comparison of modern cosmological hydrodynamic simulations see Table 1 from Tremmel et al. (2019).

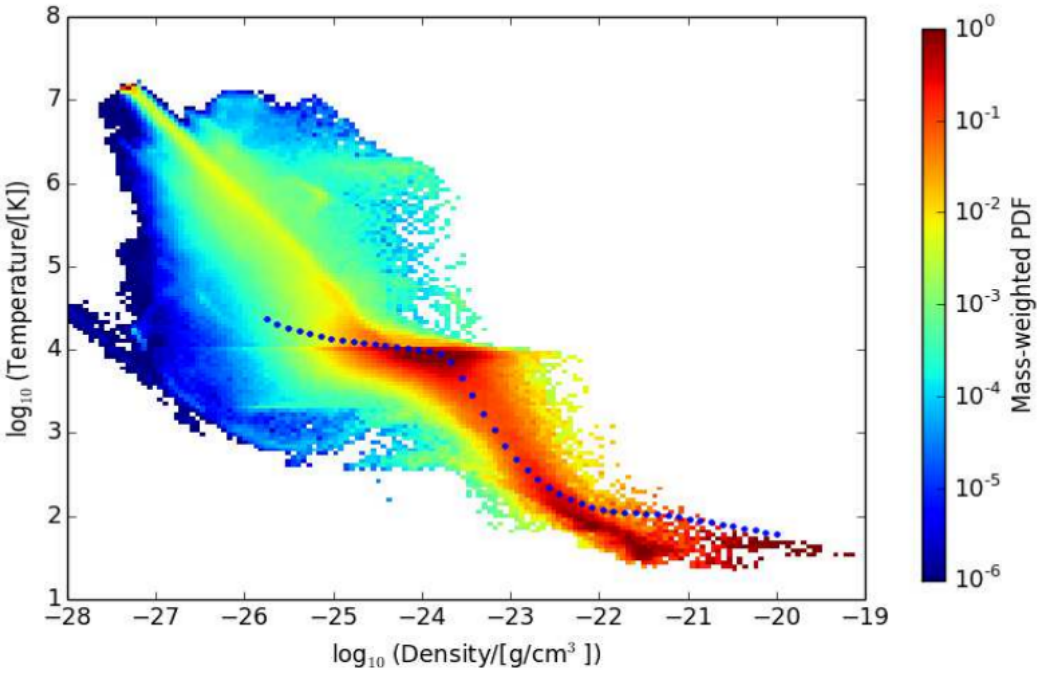

Figure 3: Mass-weighted phase space probability distribution for a simulation run with random supernova driving. The blue dotted line represents the equilibrium curve. The cutoff between the CNM and the WIM is roughly around a density of 10^{-23} g/cm^3. By mass, a significant amount of the *stable* gas is part of the CNM, however a large fraction of the gas overall is in the unstable phase (i.e., it has not settled naturally into one of the states described in Section 2.1.2) . Figure from Walch et al. (2015).

is referred to as *peak driving* in SILCC, since supernovae go off at the peaks of the density distribution). Another possibility is to place the supernovae in low density environments. Earlier feedback from stellar winds and radiation can create cavities around massive stars, so in this case supernova explosions occur in regions of lower density (this is referred to as *random driving*, because if supernova events go off in random locations in the simulation, they are more likely to occur in the hot, less dense medium occupying most of the volume). Finally there is the mixed approach, in which half of the supernovae occur at the peaks of the density distribution and half occur at random locations (*mixed driving*).

An important result is related to the filling fraction of different gas phases. The simulations show that, by mass, most of the *stable* gas is in the WIM phase, however a significant fraction of the gas overall is in an intermediate, unstable phase (Figure 3), which is also consistent with observations (Heiles & Troland,

2003). Similarly, by volume filling fraction, about half of the gas can be found in the hot phase, with a significant portion being in the unstable phase and trace amounts in the cold phase (Walch et al., 2015).

2.3 Turbulence in the ISM

Turbulence is a term used to describe chaotic motions in a fluid which dissipate energy from large to small scales. It is ubiquitous in the ISM and plays a major role in several processes such as the formation of dense structures and stars, the stability of molecular clouds, the amplification of magnetic fields, and the re-acceleration and diffusion of cosmic rays (Falceta-Gonçalves et al., 2014).

An important question is what drives the turbulence. The two main candidates are stellar feedback and gravitational instability.

2.3.1 Sources of turbulence: Stellar feedback

There are various astrophysical processes related to stellar activity that could be sources of turbulence for the ISM gas. Throughout their lifetime, massive stars release energy and momentum into their surroundings via radiation and stellar winds. Massive stars (> 8 $M_\odot$) end up as core collapse supernovae, while white dwarfs (stellar remnants of lower mass stars) in binary systems can accrete gas from their companion and explode as type Ia supernovae. The energy output of massive stars can be equal or even greater than that resulting from a supernova explosion (see Section 3.7).

In principle, the supernova rate in a galaxy like the Milky Way is sufficient to maintain ISM turbulence (Klessen & Glover, 2014). In addition to this, surveys have shown that there is a correlation between the velocity dispersion in the ISM and galaxy's star formation rate (SFR). However, simulations which only take into account supernova feedback do not find the required velocity dispersion (Krumholz & Burkhart, 2016).

2.3.2 Sources of turbulence: Gravity

There is another category of potential sources of turbulence that are related to gravity, in particular accretion.

Given the currently observed rate of star formation of ~ 1.5 $M_\odot yr^{-1}$ (Robitaille & Whitney, 2010; Licquia & Newman, 2015), the Milky Way would deplete its gas reservoir on a time scale of ~ 2 Gyr (Bigiel et al., 2008). Similar gas depletion times have been observed for other spiral galaxies (Bigiel et al., 2011). In all cases this time scale is much shorter than the ages of these galaxies. This would imply that there is an extragalactic source of gas which replenishes

the star formation process. Whether this mechanism provides sufficient energy is still a controversial topic. According to Klessen & Hennebelle (2010), accretion is sufficient to account for turbulence in galaxies, while Elmegreen & Burkert (2010) argue that accretion can only account for turbulence in the early stages of galaxy formation, which is then driven by gravitational instabilities and star formation.

Another approach, which looks at the velocity dispersion observed in the ISM, suggests that gravitational instabilities are the ultimate source of ISM turbulence (Krumholz & Burkhart, 2016).

2.4 Shocks

A shock is a transition layer which propagates through a plasma and changes it thermodynamic properties: temperature, pressure, density, entropy. The thickness of the transition layer is determined by the physical process responsible for this energy conversion. In an ordinary gas shock the energy is transferred by two-body collisions and in this case the thickness is of the order of a few collisional mean free paths. However, in the ISM the conditions are very different from laboratory plasmas. In this very tenuous medium collisions are rare and the energy is transferred through collective electromagnetic effects. These shocks are called *collisionless* and their thickness is of the order of the gyroradius of a thermal ion (or the Debye length if electrostatic effects become significant). An energetic charged particle is one which has sufficient momentum not to resonate with this electromagnetic turbulence in the shock front and thus see the shock essentially as a discontinuity (whereas the 'thermal' particles interact strongly and are 'heated') (Drury, 1983).

A more descriptive way to define a shock would be as a signal which propagates through a medium with a velocity higher than the speed of sound in that medium. The ratio between the speed of this signal and the speed of sound is called the Mach number, $\mathcal{M}$. As it moves through the gas, the shock compresses and transfers some of its energy to the plasma, essentially converting supersonic gas into denser, slower moving, higher pressure, subsonic gas.

For high Mach numbers (strong shocks), the ratio between upstream (before the shock, v_u) and downstream (after the shock, v_d) velocities is

$$\frac{v_u}{v_d} = 4 \tag{2}$$

2.4.1 Cosmic ray acceleration at shocks

Shocks play an important role in the process of accelerating cosmic rays. Even before a specific mechanism had been proposed, Fred Hoyle suggested supernova explosions could be a source on energetic grounds (Hoyle, 1946). In the following

decades, expanding on the Fermi mechanism (see Section 2.1.1), a series of studies developed a rigorous framework for the acceleration process at supernova shocks (Krymskii, 1977; Axford et al., 1977; Blandford & Ostriker, 1978; Bell, 1978a,b).

Any proposed acceleration mechanism should provide an explanation not only for the high energies charged particles achieve, but also account for the power-law distribution.

Consider a population of high energy particles in the upstream of a strong shock whose velocity distribution is isotropic in the frame moving with the gas. These collisionless particles do not feel the shock and cross into the downstream, where they encounter gas traveling at $3/4v_s$ (where v_s is the shock velocity). These particles are then scattered by resonant MHD modes downstream and receive an energy increase. Their velocity distribution also becomes isotropic in the downstream gas frame. When these particles move back into the upstream region, they once again encounter gas traveling at $3/4v_s$ and receive the same amount of energy. With every shock recrossing, after collisions with downstream and upstream magnetic mirrors, the particles receive a small amount of energy (Urošević et al., 2019). This process is called *diffusive shock acceleration*. During a large number of crossings, a charged particle can be accelerated to extremely high energies, up to a limit given by the Hillas criterion (see Section 2.1.1).

2.5 Density PDF in the ISM

The shape of the ISM density PDF is an important tool in the analysis of interstellar gas, which has been used to explain the initial mass function (IMF), star formation rate (SFR), and Kennicutt-Schmidt law. The most common view is that the density PDF of the isothermal, turbulent ISM has the shape of a log-normal (Vazquez-Semadeni, 1994; Federrath et al., 2010)

$$f(\rho)d\rho = \frac{1}{\sqrt{2\pi\sigma_\rho}} \exp\left[-\frac{(\ln\rho - \mu_\rho)^2}{2\sigma_\rho^2} \right] \frac{\mathrm{d}\rho}{\rho} \tag{3}$$

where $\mu_\rho = \ln\rho_0$, ρ_0 is the median of the density distribution and σ_0 is the width of that distribution. This property of the ISM can be explained by a process involving turbulence. It is assumed that the density distribution is generated by shocks colliding in isothermal supersonic turbulence, in a random, multiplicative process. A multiplicative process in ρ turns into an additive process in log ρ, which by the central limit theorem returns a Gaussian distribution (Federrath & Klessen, 2012).

At higher densities, where self-gravity becomes important and star formation begins, the PDF develops a power-law tail (Ballesteros-Paredes et al., 2011).

It is relevant at this point to define the clumping factor C_ρ, which is a measure of how the density varies in a medium (Owocki & Cohen, 2006)

$$\mathrm{C}_\rho = \frac{\langle \rho^2 \rangle_V}{\langle \rho \rangle_V^2} \tag{4}$$

where $\langle \rho \rangle_V$ is the volume-weighted density of the gas.

For a log-normal density distribution, the clumping factor C_ρ can be written as (Gnedin et al., 2009)

$$\mathrm{C}_\rho = e^{\sigma_\rho^2} \tag{5}$$

where σ_ρ^2 is defined as

$$\sigma_\rho^2 = \ln\left(\frac{\langle \rho \rangle_M}{\langle \rho \rangle_V}\right) \tag{6}$$

and $\langle \rho^2 \rangle_M$ is the mass-weighted density of the gas (see Buck et al., submitted to MNRAS, under review, for the full derivation). It is well-established from numerical simulations that, in the turbulent ISM, the width and peak of the log-normal density distribution (and thus also the clumping factor) depend on the Mach number $\mathcal{M}$ (see e.g. McKee & Ostriker, 2007). Other studies (Federrath et al., 2008) have shown that the clumping factor can further depend on the turbulence driving parameter b

$$C_\rho = 1 + b^2 \mathcal{M}^2 \tag{7}$$

which which takes the values b $\sim$ 1 for compressive driving and b $\sim$ 1/3 for solenoidal driving.

2.6 Molecular clouds and star formation

It is a basic astrophysical fact that stars form from gas in the ISM. Studies have shown that there is a correlation between the *total* gas surface density and the SFR surface density. This correlation has the form of the power-law with an index N $\sim$ 1.5 and known as the *Kennicutt-Schmidt law* (Schmidt, 1959; Kennicutt, 1998). More recent work has shown that, in fact, the strongest correlation is between the star formation rate and the surface density of *molecular gas* and that there is virtually no correlation between atomic hydrogen and star formation (Bigiel et al., 2008; Leroy et al., 2008). This is why it is important to first summarize the properties of molecular clouds and then go into how star formation happens, in particular massive stars.

2.6.1 Molecular cloud properties

Molecular clouds are the coldest, densest regions of the ISM ($n \sim 10^1 - 10^5$ cm^{-3}, T$\sim$ 10 K). They are observed to have a wide range of masses, from a few $M_\odot$ to $\sim 10^7$ $M_\odot$ (Miville-Deschênes et al., 2017). The cloud mass spectrum is well-fit by a power-law with index $\gamma \sim 1.6 - 2$

$$\frac{dN}{dM} \sim M^{-\gamma} \tag{8}$$

Although different studies have shown slight differences in the value of γ for molecular clouds in the Milky Way (Solomon et al., 1987; Williams & McKee, 1997; Roman-Duval et al., 2010), since it is consistently < 2 this implies that most of the mass can be found in the highest mass clouds. The surface density of molecular clouds is $\sim$ 100 $M_\odot \cdot$ pc^{-2}, an order of magnitude larger than the highest surface densities observed for HI gas.

Similarly to the rest of the gas in the ISM (and for similar considerations, see Section 2.3) surface densities in molecular clouds have been shown to follow a log-normal PDF with a power-law at higher densities. It is important to note however that power-law tails are observed particularly in star forming gas clouds, where self-gravity becomes important, while in clouds without active star formation the log-normal shape of the surface density PDF is preserved (Kainulainen et al., 2009).

Star formation efficiency is a parameter which denotes the fraction of the gas (within the galaxy or a cloud) which is turned into stars as an effect of gravitational collapse

$$\epsilon_{\rm ff} = {\rm SFR}/({\rm M_{gas}}/{\rm t_{ff}}) \tag{9}$$

where M_{gas} is the total gas mass and $t_{\rm ff}$ is the free fall time for the system

$$t_{\rm ff} \sim \frac{1}{\sqrt{G\rho_0}} \tag{10}$$

For $\epsilon_{\rm ff} \sim 0.01$, it would take a cloud 100 free fall times to convert all its gas into stars (Krumholz & Tan, 2007; Kennicutt & Evans, 2012). However since molecular clouds have lifespans that are shorter than this time, this suggests most of the gas is dispersed before being converted into stars, potentially by stellar feedback or as a result of interstellar gas flows (Larson, 2003).

2.6.2 Larson's laws

A systematic and highly influential survey by Larson (1981) has established a series of scaling relations between various properties of molecular clouds nowadays known as *Larson's laws*.

Linewidth size relation According to the linewidth-size relation, the velocity dispersion (i.e., the three-dimensional rms velocity of all internal motions in molecular clouds) is proportional to the size of the clouds. Larson (1981) found this relation to be $\sigma = 1.10 L_{pc}^{0.38}$, where σ is the velocity dispersion and L_{pc} is the size of the cloud in units of parsecs, and notes that it is valid for clouds between 0.1 to 100 parsecs. Subsequent studies have obtained similar results, e.g. Solomon et al. (1987) finding $\sigma = 1.0 \pm 0.1 L_{pc}^{0.5 \pm 0.05}$, while Heyer & Brunt (2004) found $\sigma = 0.9 \pm 0.19 L_{pc}^{0.56 \pm 0.02}$.

Note that the exponents are very close to the scaling $\sigma(\ell) \sim \ell^{0.5}$ which is expected from supersonic turbulence (McKee & Ostriker, 2007).

Velocity dispersion is proportional to cloud mass The virial parameter is defined as

$$\alpha = \mathrm{a} \frac{2\mathrm{T}}{|\mathrm{W}|} = \frac{5\sigma \mathrm{R}}{\mathrm{GM}}$$

where T is the kinetic energy of the internal motions in an astrophysical object, W is the gravitational potential energy, σ is the velocity dispersion, R is the characteristic size of the object, M is the mass, G is the gravitational constant, and a is a factor of order unity[4] which accounts for the internal structure and shape of the cloud (see e.g. Miville-Deschênes et al., 2017, Appendix D). Larson found that molecular clouds are approximately in virial equilibrium, i.e. $\alpha \sim 1$, which implies there is roughly a balance between gravitational energy and turbulence.

Cloud size is inversely proportional to density The linewidth-size relation implies that, in order to be gravitationally bound, smaller clouds must have higher densities (Larson, 1981). Taking the first two laws together, it follows that cloud size is inversely proportional to density, i.e. that there is a characteristic column density for all clouds. This value was first computed by Solomon et al. (1987), who found it to be 170 $\mathrm{M}_{\odot} \cdot \mathrm{pc}^{-2}$. Recomputing the data from the Solomon et al. (1987) sample assuming a galactocentric radius for the Sun of 8.5 kpc instead of 10 kpc, Heyer et al. (2009) found the median surface density to be 206 $\mathrm{M}_{\odot}$ pc^{-2} and then presented their own estimate, computed using a different method, for the surface density to be 42 $\mathrm{M}_{\odot}$ pc^{-2}. Note that Roman-Duval et al. (2010) found a median surface density of 144 $\mathrm{M}_{\odot}$ pc^{-2}. The universality of this relation has been challenged however. Recent observations have found surface densities

[4]Observed values of the virial parameter are found in the range 1-100, which suggests that not all clouds are actually in virial equilibrium (Miville-Deschênes et al., 2017)

in the range 2-300 $M_\odot$ pc^{-2}, with a mean value of ~ 30 $M_\odot$ pc^{-2}, which increases towards the inner galaxy (Miville-Deschênes et al., 2017).

2.6.3 Giant molecular cloud formation

With regards to the formation of giant molecular clouds (GMCs), there are two main aspects to consider: chemical and dynamical (i.e., how the H_2 molecules form and how the clouds themselves are assembled within the ISM).

H_2 molecules form from the combination between two hydrogen atoms. However the simple reaction between hydrogen atoms or ions which lead to the formation of H_2, such as $H + H \longrightarrow H_2 + \gamma$ (where γ represents a photon) are highly inefficient in the ISM, in particular at the low temperatures of the CNM. Instead, H_2 forms on the surface of dust grains (Gould & Salpeter, 1963; van Dishoeck & Black, 1986). The formation rate depends on the density of gas particles and hydrogen atom particles (which can be taken to be identical by neglecting helium and heavier elements), with a timescale of (Girichidis et al., 2020)

$$\mathrm{t_{form}} = \frac{\mathrm{n_H}}{\mathrm{R_{H_2}}} 10^9 \mathrm{n^{-1}yrs} \tag{11}$$

where n_H is the hydrogen number density, n is the gas number density, and R_{H_2} is the H_2 formation rate according to Jura (1975). While at low densities this time scale is longer than the dynamical timescale of the system (the gravitational free-fall time or the turbulent crossing time), compression from supersonic turbulence can shorten H_2 formation time sufficiently so that it occurs within the expected time frame.

The second issue with regards to GMC formation is how clouds form as distinct structures within the ISM. It is important to note that molecular clouds are different from other astrophysical objects such as stars and galaxies in the sense that they are not quasi-equilibrium structures. Rather they are transient features

2.7 Massive star formation

Stars are the fundamental building blocks in many areas of astrophysics. A significant part of the (baryonic) mass in typical galaxies is in the form of stars and most of the radiation is emitted by them. For this reason, it is very important to understand the processes which lead to star formation. Massive stars in particular play a very important role in the processes which determine the properties of the ISM, e.g. heating, metal enrichment, CR acceleration, and are responsible for feedback processes that influence further star formation (Tan et al., 2014).

In addition to turbulence, gravity and pressure are the main factors which determine the dynamic state of an astrophysical gas. In fact, the end state in

the star formation process is achieved when pressure balances gravity. Until that point is reached however, it is important to explain why a self-gravitating gas starts to collapse in the first place. This is a classical problem in astrophysics, which was rigorously treated by James Jeans at the beginning of the 20th century (Jeans, 1902). Jeans found a hydrodynamical instability in the self-gravitating gas characterized by a length scale called the *Jeans length*

$$\lambda_J = \sqrt{\frac{\pi c_S^2}{G\rho_0}} \tag{12}$$

where G is the gravitational constant, ρ_0 is the characteristic density of the gas and c_S is the sound speed in the gas. One can also derive a characteristic *Jeans mass*, i.e. the mass contained in a volume with a radius of the Jeans length (Krumholz, 2015; Girichidis et al., 2020)

$$M_J = \frac{4\pi}{3}\rho_0\left(\frac{\lambda_J}{2}\right)^2 = \frac{\pi^{5/2}}{6}\frac{c_S^3}{(G^3\rho_0)^{1/2}} \tag{13}$$

The physical interpretation of the the Jeans length is that clouds larger than this scale cannot be supported by pressure and will start to collapse under the effect of gravity on a dynamical (free-fall) timescale (Equation 10).

This simple argument can explain why gravitational collapse occurs, however star formation is a complex process which usually happens within clusters and is therefore influenced by feedback, rather than being an isolated event. In the case of massive stars, there the two main models which explain their formation: the *core accretion* model and the *competitive accretion* model (Krumholz & Bonnell, 2007; Tan et al., 2014).

Core accretion model According to the core accretion model, stars form from a core with a mass that is related to the final mass of the star, i.e. it is a scaled up version of how a low-mass star would form (Krumholz & Bonnell, 2007). The process starts with self-gravitating, centrally concentrated cores of gas, which undergo gravitational collapse to form either a single star or a multiple system (Tan et al., 2014).

Competitive accretion model In a competitive accretion model, gas is initially funnelled into the central gravitational potential, where fragmentation leads to the formation of low-mass stars. High-mass stars subsequently form as they accrete the gas which continues to stream towards the center of the potential, where the most massive proto-stars are located (Bonnell et al., 2001).

2.8 Stellar winds

In addition to radiation, stars interact with their surroundings mainly via stellar winds, providing mechanical (momentum) and chemical feedback on the ISM throughout the lifetime of the star. Mass loss via stellar winds is particularly important in massive stars, i.e. with $M > 8M_{\odot}$. In this case, mass loss can be significant enough to have an effect on the evolution of the star (as in the case of Wolf-Rayet stars, see e.g. review by Crowther, 2007), on the surrounding gas (creating a cavity in the ISM called a "wind-blown bubble", see e.g., Weaver et al., 1977), and on the mass of the stellar remnant (see e.g. Belczynski et al., 2020, who show how the mass of a black hole can vary dramatically depending on the mass loss rate of the progenitor star).

2.8.1 Stellar wind formation in massive stars

Early theories on the origin of stellar winds were put forward by Parker (1958, 1960), who explained that the outer layers of a star like the Sun expand under the effect of thermal pressure. The outer layers of the star (the *corona*) are heated to temperatures on the order of 10^6 K making them expand and generating a pressure-driven wind.

In hot, massive stars however, radiation pressure alone is not sufficient to account for the observed high mass loss rates, which can be on the order of $10^{-5}M_{\odot}yr^{-1}$. Instead these stellar winds are radiation driven, usually referred to as *line-driven winds* (Castor et al., 1975).

The mechanism can be summarized as follows. A photon is absorbed in an atomic transition if its energy corresponds to the difference in energy levels of the atom it interacts with. The atom briefly goes into an excited state and then returns to its original energy level, re-emitting a photon of equal energy with the one it absorbed. During this process, energy and momentum are transferred back and forth from the radiation field to the (ionized) gas in the stellar atmosphere. The key to driving stellar winds in this scenario is that the gas is accelerating. While in a plasma moving with constant velocity the number of photons with energy corresponding to a transition in the particle is limited, in an accelerating plasma the photons are Doppler shifted with respect to the ions, which means that they are constantly able to absorb a steady flux of photons which have been absorbed and re-emitted in the layers below, leading to further acceleration. This is what is known as *line force* and is responsible for driving the strong winds observed to come from massive stars. It is also important to note that, although hydrogen and helium are the most abundant elements in the stellar atmosphere, metals (in particular iron) have a significantly larger number of atomic transitions and therefore are much more important for this process (Puls et al., 2008; Muijres,

2010).

The classical theory of how stellar winds influence the ISM comes from the work of Weaver et al. (1977). In this picture, isotropic stellar winds from a massive star create a cavity around it filled with hot gas ($T \geq 10^6$ K, sufficient for X-ray emission) which expands adiabatically. The interstellar gas is swept up and compressed into a thin shell which is expanding with a velocity greater than the local sound speed, creating a shock (see Section 2.4). The radius of this bubble scales as $R_b \propto t^{3/5}$.

2.8.2 CR acceleration at stellar wind shocks

The main source of CRs in the galaxy is though to be massive stars, in particular the supernova shocks created at the end at their lifetime. However it is well-established that CRs can also be accelerated at stellar wind termination shocks (Webb et al., 1985). The question of the relative importance of these sources has been recently studied by Seo et al. (2018). Using stellar wind models from Georgy et al. (2012), the authors estimate that the stellar wind luminosity is about a factor of 3 smaller than the supernova luminosity in the galaxy. However, while supernovae accelerate CRs with an efficiency of $\sim 10\%$ (i.e., about 10% of the supernova energy is transferred to CRs), stellar wind shocks are assumed to have an efficiency $\sim 1 - 10\%$. While supernova shocks still appear to be the main source of galactic CRs, stellar wind shocks may still play an important role in the acceleration process, in particular in young clusters where no supernova explosions have occurred.

3 Methods

In this section we analyze the ISM in terms of the average density and column density evolution as gas structures form. For this we use data from the SILCC simulation (for details about the simulation see Section 2.2)

Simulation resolutions are: 0.5 pc, 1 pc, 2 pc, and 4 pc. Throughout this report we will first describe the analysis of the 1 pc simulations, and compare it to the data obtained from the 2 pc simulations. Snapshots are available spanning a physical time of 60 Myrs (snapshot at $t = 0$ is missing for the 1 pc simulation), at intervals of 10 Myrs. For the highest resolution simulation only three snapshots are available at physical times between 20 and 21 Myrs, 0.2 Myrs apart.

3.1 Characterizing the ISM

The data analysis is performed using the `healpy`[5] and `yt`[6] packages, as well as the standard Python packages `numpy` and `matplotlib`.

Since our aim is to characterize the ISM in spherical regions, it is convenient to use the HEALPix (Gorski et al., 2005) tessellation of the sphere. HEALPix divides the surface of the sphere into quadrilateral, curvilinear pixels of varying shapes and equal areas. The resolution depends on the N_{side} parameter, i.e. $N_{pix} = 12 \times N_{side}^2$. The N_{side} parameter must be a power of two. In our analysis we used HEALPix resolutions 4, 8, and 16, corresponding to 192, 768, and 3072 pixels on the sphere surface.

For our analysis we investigate the properties of density structures in the ISM, focusing on different quantities which we will describe in this section. The sphere density ρ_S is the volume average density of an individual sphere,

$$\rho_S = \frac{M_R}{V_R} \tag{14}$$

where M_R is the total mass enclosed in the sphere and V_R is the volume of that sphere, for a particular radius R.

The number of data points depends on the sphere radius used. The average density ρ is the average of all the sphere densities,

$$\rho = \frac{\sum_i^N \rho_{S_i}}{N} \tag{15}$$

[5] https://healpy.readthedocs.io/
[6] https://yt-project.org/

where N is the total number of spheres sampled. This parameter is representative of the entire snapshot. Column density Σ is defined as the mass per area for a single column within a sphere,

$$\Sigma = \frac{\sum_{j}^{K} m_j}{A} \tag{16}$$

where K is the number of mass cells along a line of sight and A is the surface area of that pixel. Note that a potential issue that could arise is that a coarser division of the surface of the sphere could mean that more cells overlap with each HEALPix pixel, which would lead to the average column density being higher with lower values of the N_{side} parameter. We sought to mitigate this effect by dividing the total mass along a line of sight equally to the number of pixels which overlap with it.

The median sphere column density Σ_S is the median column density for an entire sphere

$$\Sigma_S = \Sigma^{50} \tag{17}$$

and Σ_a is the average column density per snapshot

$$\Sigma_a = \frac{\sum \Sigma_S}{N} \tag{18}$$

We define a width parameter to describe the distribution of column densities on the sphere,

$$\omega_{16}^{84} = \Sigma^{84} - \Sigma^{16} \tag{19}$$

where Σ^{16} and Σ^{84} represent the column density values for the 16th and the 84th percentile columns, respectively. This is a measure of how uniform the gas distribution is within the volume of a sphere.

We introduce a *covering fraction* parameter, κ. It is defined as the number of lines of sight within a sphere where the column density is **above** a certain threshold value, divided by the total number of lines of sight within that sphere (in our case this corresponds to HEALPix pixels).[7]

In order to sample spheres for each snapshot, we first divide the domain into a grid of equally spaced points at a fixed distance from one another. We divide the domain into spheres centered on these points. For this part of our analysis, we used spheres of radius $R = 25$ pc as a reasonable average scale corresponding

[7]Note that we define the covering fraction in terms of the particles cm^{-2} instead of g cm^{-2}. Since the goal of our analysis is the prediction of the optical thickness of the ISM as a function of density, we chose to follow the usual convention when describing this property.

to the typical size of a GMC, which allows us to have a large enough sample of spheres in a 500 pc box, while also covering a significant enough volume within the domain. In order to avoid an issue at the boundaries where cells beyond the limits of the box are counted as empty (i.e., periodic boundary conditions are not recognized by the analysis script), we introduced a padding at the edges of the domain equal to the radius of the spheres.

The analysis procedure can be summarized as follows:

- Choose a random point from the grid covering the domain as the center of one of the spheres.
- Using the HEALPix tessellation divide the surface of the sphere into cells of equal area. Divide the sphere into columns (lines of sight) starting from the point in the center and ending on the surface cell.
- Perform this task for a statistically significant number of points within the domain. The same number of spheres (500) are sampled for for each radius, meaning that for larger spheres there will be significant overlap.
- The data is saved as a separate file for each snapshot, sphere radius, and sphere tessellation. The file contains the following data: the density of each sphere; an array of column densities for each sphere; the average and the median column density for each sphere; the position (i.e., the coordinates of the center) of each sphere.

We perform this analysis for each available simulation snapshot. For the lowest simulation resolution, i.e. 4 pc, we did not run the analysis with 10 pc spheres, since in this case the number of cells per radius is too small.

3.2 Analysis

In this section we report our most significant findings. In particular, we describe the relation ρ_S and Σ_S, the time evolution of these parameters, and the effect of changing the simulation and HEALPix resolution. We also describe the results for the covering fraction, κ, and check whether there is a relation between this parameter and ρ_S, and propose a simple function to fit this relation.

3.2.1 Density-column density relation

One application of this analysis is to determine the evolution of the average density and column density in the simulations and characterize structures forming from the hydrogen gas at different resolutions. For the 1 pc resolution simulation,

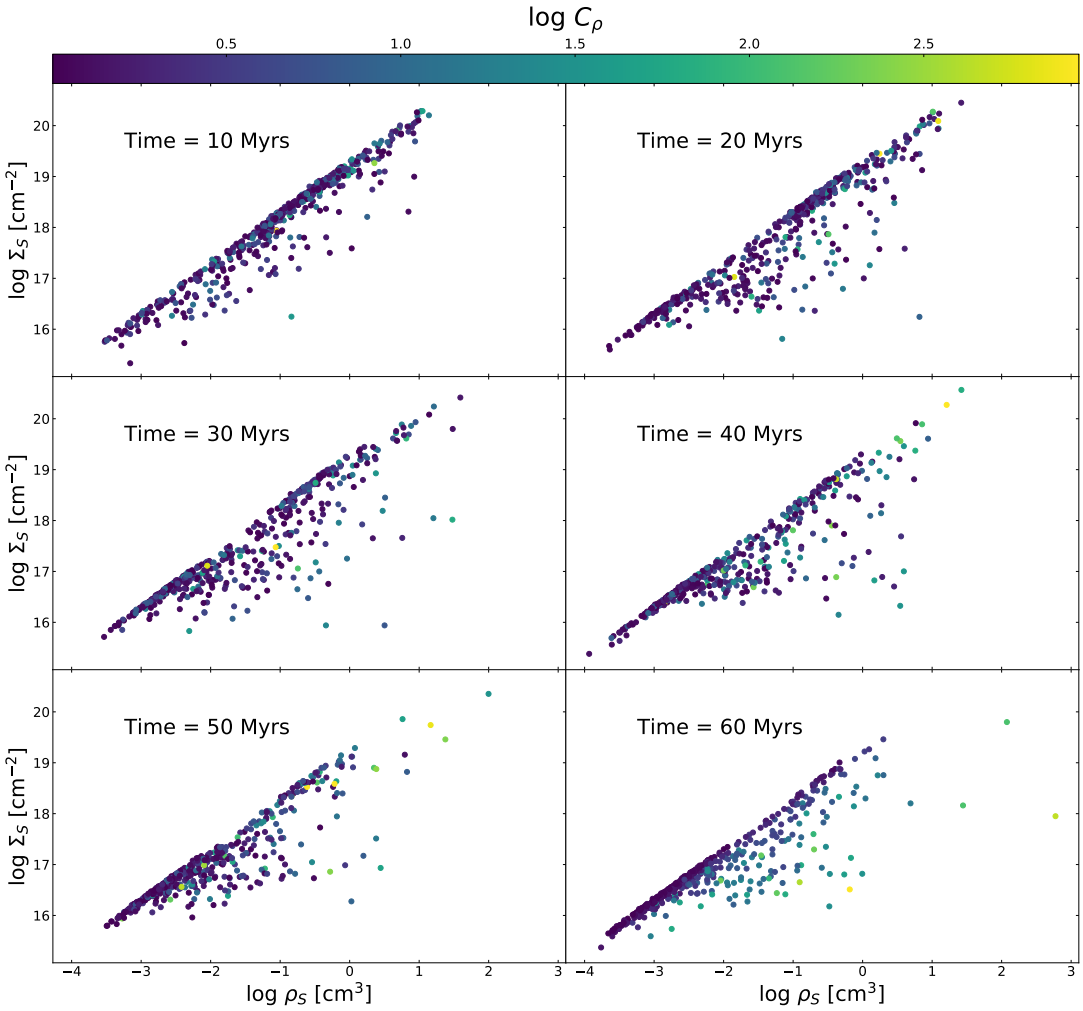

Figure 4: Evolution of the relation between Σ_S and ρ_S for the 1 pc simulation, with R = 20 pc spheres and $N_{side} = 4$. Time is shown in each subplot. Color coding denotes the clumping factor for each sphere.

which we are using as our standard run, we sample 500 spheres with radius of 25 pc at random points in the domain.

We check for a correlation between ρ_S and Σ_S. Figure 4 shows the relation between the average density and the median column density in each sphere. There is a clear pattern showing Σ_S increasing with ρ_S. The relation is linear in *log-log* space, however there are outliers, particularly as ρ_S increases.

This suggests that there is a maximum Σ_S for every ρ_S and that, at lower densities, the medium is more uniform, while at higher densities there is more variation. The color coding of spheres in Figure 4 according to C_ρ supports this

conclusion: the spheres characterized by a smaller clumping factor are located along the linear relation, while the spheres characterized by a larger clumping factor are the outliers.

We also check the evolution of the column density *width* parameter ω_{16}^{84} as a function of ρ_S. Figure 5 shows how, at early times, there is a high degree of non-uniformity in both density and column density space, with no pattern clearly visible. At later times the width decreases, and we find an increasing number of points towards the lower width, lower density end of the plots. This suggests that, with time, an increasing volume of space in the ISM consists of uniform, low density regions. We find that for every average density there is a minimum width which increases with ρ_S, implying that higher density regions are less uniform. There is also an apparent "gap" in the data for the lowest values of ω_{16}^{84} at intermediate densities of $\sim 10^{-26} - 10^{-25}$ g cm^{-3}. This implies that, after a point in the evolution of the ISM gas, regions characterized by this range of densities are significantly less uniform than both regions which are more dense and those which are less dense[8].

3.2.2 Evolution of average density and column density

We now look at how ρ and Σ change with time. Figure 6 shows how ρ decreases with time. This effect occurs for every sphere radius and HEALPix resolution, and also for other simulation resolutions. While we would not expect, in general, the average density in the entire domain to decrease (since there are no particle sinks or any other kind of mass loss mechanisms), this result can be explained by the method with which we chose to measure this quantity, i.e. by sampling spheres from random locations within the domain. With time, as structures form, more of the volume is comprised of underdense voids (see also Figure 7). This means that more spheres will be sampled from the underdense regions at later times in the simulations. In the future it may be illustrative to further quantify this finding by determining the power spectrum or structure function of density fluctuations.

In addition to the trend in ρ, the analysis shows a clear difference between the values of this parameter determined using different sized spheres. Larger spheres tend to be denser than smaller ones. This is also consistent with our explanation: sampling more distinct, smaller spheres (compared to the larger spheres, which overlap to a significant degree) within the domain tends to find a lot more spheres which are located in voids, which skews the value of ρ we determine in this manner towards the lower values.

[8]We have observed similar gaps in data with R=10 pc radius spheres, $N_{side} = 8$ in the 2 pc simulation. Further work is required in order to determine whether this is a robust phenomenon or a systematic effect of the analysis.

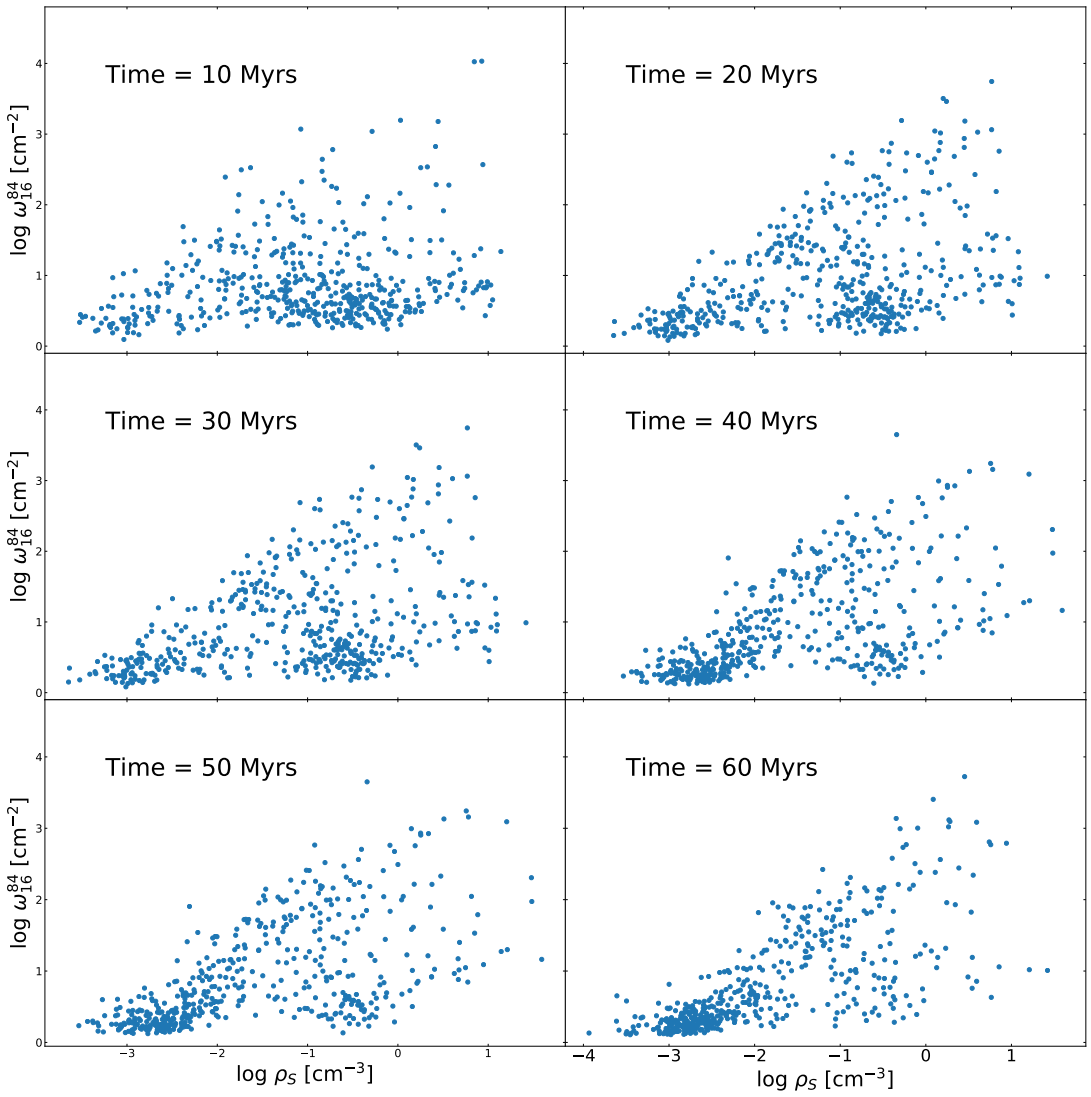

Figure 5: Evolution of ω_{16}^{84} as a function of ρ_S for the 1 pc simulation, with R = 20 pc spheres and HEALPix resolution $N_{side} = 4$. Time is shown in each subplot.

We would not expect that HEALPix resolution influences these results, since density is computed directly for every sphere. For smaller spheres any small discrepancies are likely the result of sampling. For larger spheres (R = 50pc), the differences appear more significant, however there is no clear trend showing average density being larger or smaller for a particular N_{side} parameter. This is likely also an artefact of the sampling, since a smaller number of spheres are used, the effect appears more pronounced.

Earlier in this section we explained that the decrease in ρ and Σ_a can be explained by structure formation and the growth of voids in the simulation domain. This is clearly illustrated in Figure 7, which shows the projected density along the z axis for all 1 pc resolution simulation snapshots at different points in time. Effectively, this is the column density as observed from above the x-y plane of the simulation. The top left subplot shows a mostly uniform domain. As the simulation evolves three voids become clearly visible and end up covering most of the volume. Overdense regions also appear, however they cover a significantly smaller volume.

The difference in column density between the overdense gas clumps and the voids is ~ 6 orders of magnitude. This is consistent with our results using sphere column density, as shown in Figure 4.

3.2.3 Covering fraction

The covering fraction κ is a measure of how many lines of sight within a sphere are characterized by a particle number density above a chosen threshold. Thus a sphere with covering fraction equal to 0 has no lines of sight with particle density above the threshold value (is optically *thin*), while in a sphere with covering fraction equal to 1 all lines of sight have particle number density above the threshold value (is optically *thick*).

First we plot the covering fraction as a function of different column density thresholds. Figure 8 shows this evolution for a single snapshot. As the average density of the spheres increases, the average column density also increases. This means that there are more lines of sight with column density *above* the threshold, so the value of κ is larger. This is consistent with the expectation that denser regions are more optically thick. The selection of the threshold value is also important. In our analysis, there were no spheres with a covering fraction above 0 for a threshold value of 10^{22} particles per cm^2. While this will depend on the size of the sphere we choose, the 10^{22} particles per cm^2 appears to be an upper limit in all the cases we have analyzed (i.e., spheres with radius of 10, 25, and 50 pc).

As for the density to median column density relation described before, we find that for each value of the covering fraction there is a minimum density associated

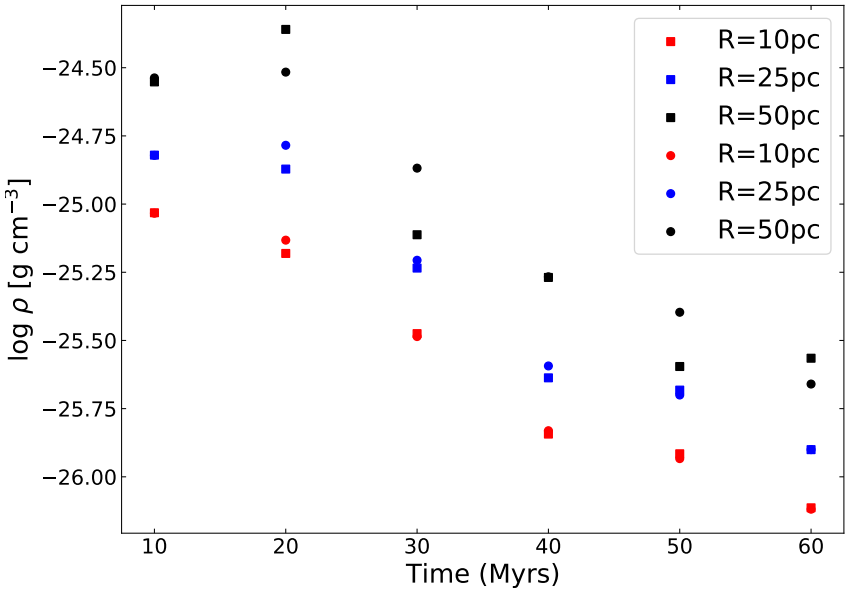

Figure 6: Average gas density in the 1 pc simulation. Colors represent different sphere radii. Different N_{side} parameter values are denoted by different markers: circles and squares correspond to HEALPix resolutions of 4 and 8, respectively. With the exception of some outliers, there is a clear decreasing trend in the average density. There is also a difference in average density between the 10 pc and 50 pc of 0.5-0.6 dex, corresponding to a factor of 3-4, the larger spheres showing a larger average. This is a result of the sampling of spheres (see text for explanation).

with it. However the range of densities for a given covering fraction can span $\sim 2-3$ orders of magnitude. This is consistent with the conclusion that higher density regions are are more structured than lower density regions.

3.2.4 Comparing results with different HEALPix resolutions

We check whether the density or the column density are different or evolve differently depending on the HEALPix resolution. For this we compare the results obtained using different values of the N_{side} parameter.

We begin by checking the time evolution of the column density Σ_a. Figure 9 illustrates the time evolution of Σ_a using R= 25pc spheres, for the 1 pc and 2 pc simulations. In both cases, there is a linear decrease with time, corresponding

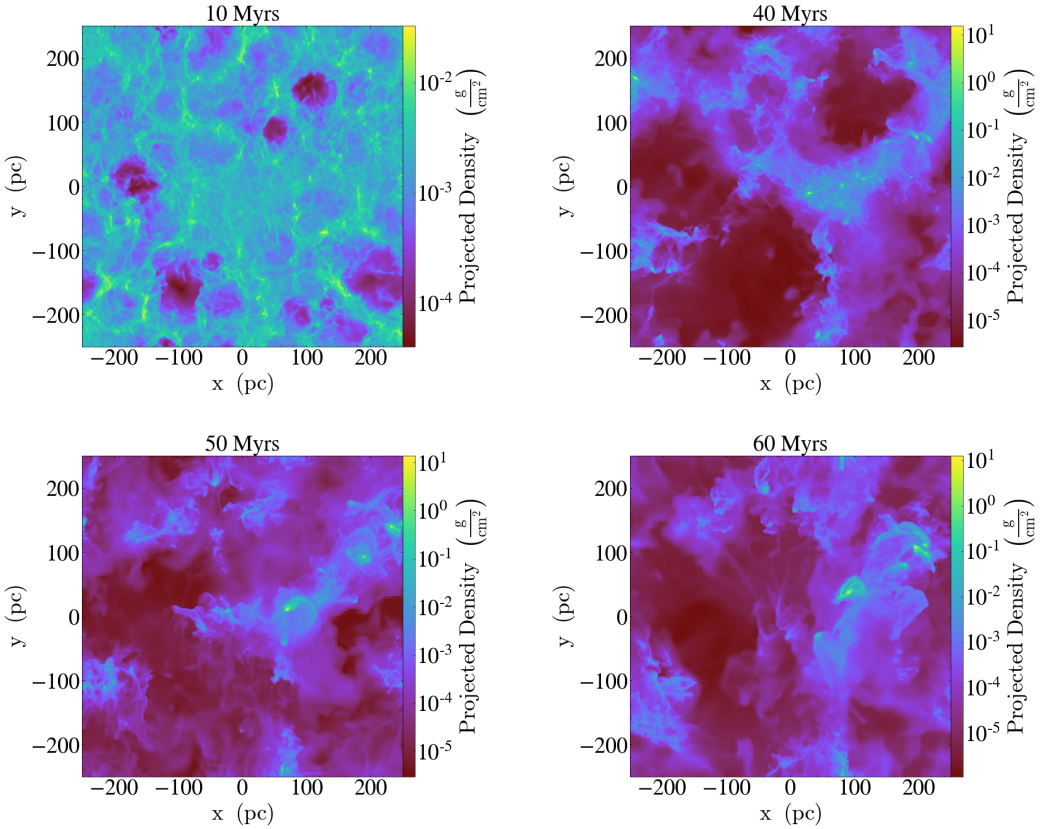

Figure 7: Projected density along the z axis for the 1 pc simulation snapshots at different simulation times (denoted in the plot title). Initially the medium is uniform, with a few underdensities. These underdensities grow in size and dominate the medium by the end of the simulation time.

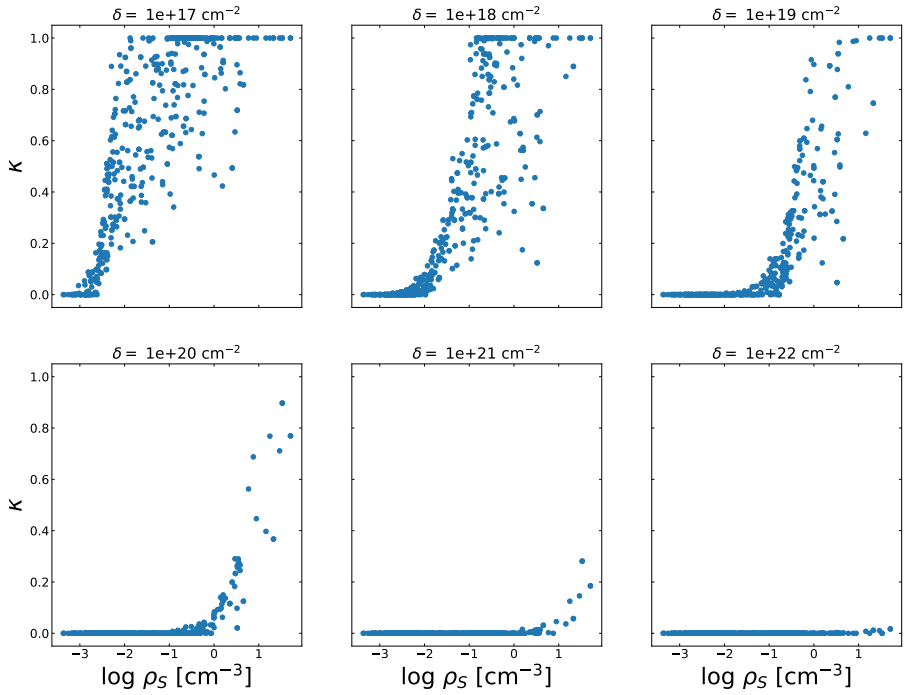

Figure 8: Evolution of κ as a function of density ρ_S with different threshold values. As the threshold parameter δ increases, there are fewer lines of sight for every sphere with column density higher than the chosen value. The figures in the lower panel represent threshold values which are higher than those typically found in the ISM.

to an order of magnitude, of this parameter. This decrease is apparent for all HEALPix resolutions, as well as for the 1 pc and 2 pc simulation resolutions. For the 0.5pc simulation resolution, the time interval between snapshots is 0.2 Myrs, not enough to observe any evolution. Differences between points representing HEALPix resolutions are small and there does not appear to be any systematic pattern in the variation.

When comparing the results obtained using different N_{side} parameters, we noticed only small variations in the value of Σ_a. Table 2 shows the ration between Σ_a when dividing sphere surfaces using different HEALPix resolutions, for both the 1 pc and 2 pc simulations. Ideally we would expect the average column density to be independent of HEALPix resolution. This appears to be the case for the 2 pc simulation, where the Σ_a ratios are close to unity, while the average ratio across

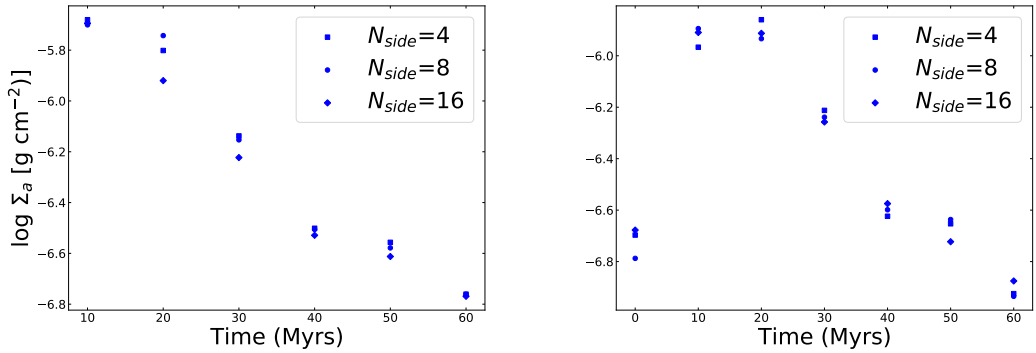

Figure 9: Average column density evolution for two simulation resolutions: 1 pc (*left*) and 2 pc (*right*). Circles, squares and diamonds represent HEALPix resolutions of 4, 8 and 16, respectively. The sphere radius is R= 25pc in all cases.

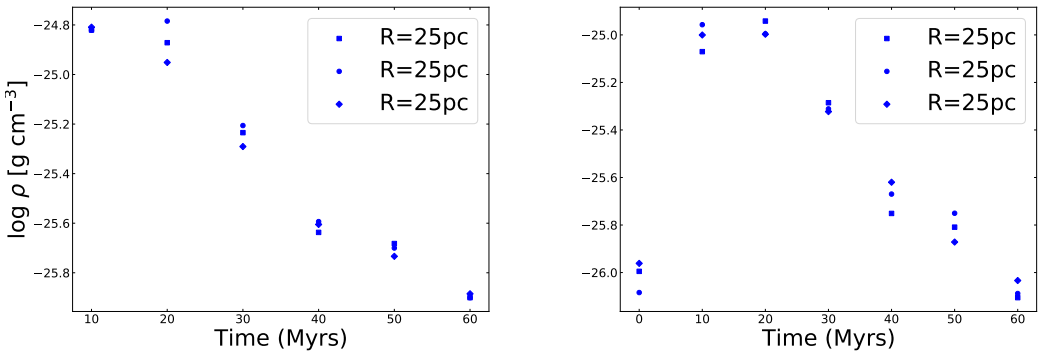

Figure 10: Average density evolution for two simulation resolutions: 1 pc (*left*) and 2 pc (*right*). Circles, squares and diamonds represent HEALPix resolutions of 4, 8 and 16, respectively. The sphere radius is R= 25 pc in all cases.

all snapshots is 1.00. For the 1 pc simulation, the Σ_a ratio is consistently higher than unity, suggesting a higher HEALPix resolution results in higher average column densities.

We have also found that ρ tends to decrease with time. As in the case of Σ_a, Figure 10 illustrates this evolution for all HEALPix resolutions. For both Σ_a and ρ, the small variations observed when varying the N_{side} parameter are likely due to differences in sampling, since for every analysis run the sphere centers are different random points on an equally spaced grid.

Snapshot	Ratio of Σ_a values between $N_{side} = 16$ and $N_{side} = 4$	Average ratio for simulation resolution
0000	0.96	
1000	0.88	
2000	1.13	
3000	1.11	1.00
4000	0.89	
5000	1.17	
6000	0.89	

Snapshot	Ratio of Σ_a values between $N_{side} = 16$ and $N_{side} = 4$	Average ratio for simulation resolution
1000	1.03	
2000	1.31	
3000	1.22	
4000	1.07	1.13
5000	1.14	
6000	1.02	

Table 2: Ratio of Σ_a for data obtained with spheres using parameters $N_{side} = 16$ and $N_{side} = 4$. Different HEALPix resolutions result in cells of different surface areas. However the data in this table shows that, when converting from HEALPix cell area to cm^2, there is almost no variation in Σ_a between different simulation snapshots. *Top*: Ratios and average ratio for the 2 pc simulation. This is very close to the expected value. *Bottom*: Ratios and average ratio for the 1 pc simulation.

3.3 The clumping factor

We introduced the clumping factor parameter in Section 2.5 (see Equation 4). In addition to the standard, *volume* clumping factor, it is possible to also compute a *projected* clumping factor, which is essentially a clumping factor of column densities. The relation between the volume clumping factor and the projected clumping factor can be written as (the complete derivation can be found in Buck et al., submitted to MNRAS, under review)

$$C_\Sigma = C_\rho^{2/3} \tag{20}$$

It is useful to derive a relation between the characteristic (median) column density Σ_0 and other relevant parameters

$$\Sigma_0 = \frac{R}{3}\frac{\langle\rho\rangle_V}{C_\Sigma^{1/2}} \tag{21}$$

where R is the radius of each sphere, $\langle\rho\rangle_V$ is the volume weighted average density, and C_Σ is the column density clumping factor.

3.4 Density to column column density relations

As we have already seen, there seems to be a rough linear relation between column density and volume density with a lot of scatter. However this variation lies below a diagonal. This linear relation represents the spheres that are the most uniform. One way to explain this is with the following argument: uniform spheres contain matter that is distributed evenly, so an increase in volume density is followed by a corresponding increase in surface density. Spheres that lie along this diagonal are thus expected to be characterized by the lowest clumping factor. On the other hand, the spheres found below this line are expected to be more structured. An increase in density means that the extra matter will not be distributed evenly to all lines of sight within the sphere. This pattern is highlighted in Figure 11, which shows the same relation between ρ_S and Σ_S, with color coding for the clumping factor for each sphere. Superimposed onto each plot are a series of lines representing the relation from Equation 21.

To further illustrate this idea, we also look at a projection of the gas from the SILCC simulation. Figure 12 shows gas density projections along each of the three axes, where the locations of four spheres with R = 20 pc have been highlighted. The bottom left panel shows a plot similar to those in Figure 11, with the same four spheres also highlighted. As expected, the spheres along the linear relation represent the more uniform regions, while the spheres which that are found below this line are increasingly more structured.

This can also be observed from the histograms of the highlighted spheres from Figure 12 as shown in Figure 13. The first two panels (upper row) represent the higher density spheres (red and magenta on the density projection plots). They are characterized by higher average densities, as well as higher distribution widths. The other panels (bottom row) represent lower density spheres (cyan and orange on the density projection plots). They are not only lower density (as shown by the lower values for the mean and median densities), but are also more uniform (lower width of the column density distributions).

3.5 From the column density PDF to covering fraction

We have already seen that the ISM PDF is characterized by a log-normal shape (see Section 2.5, in particular Equation 22). Under the assumption that the

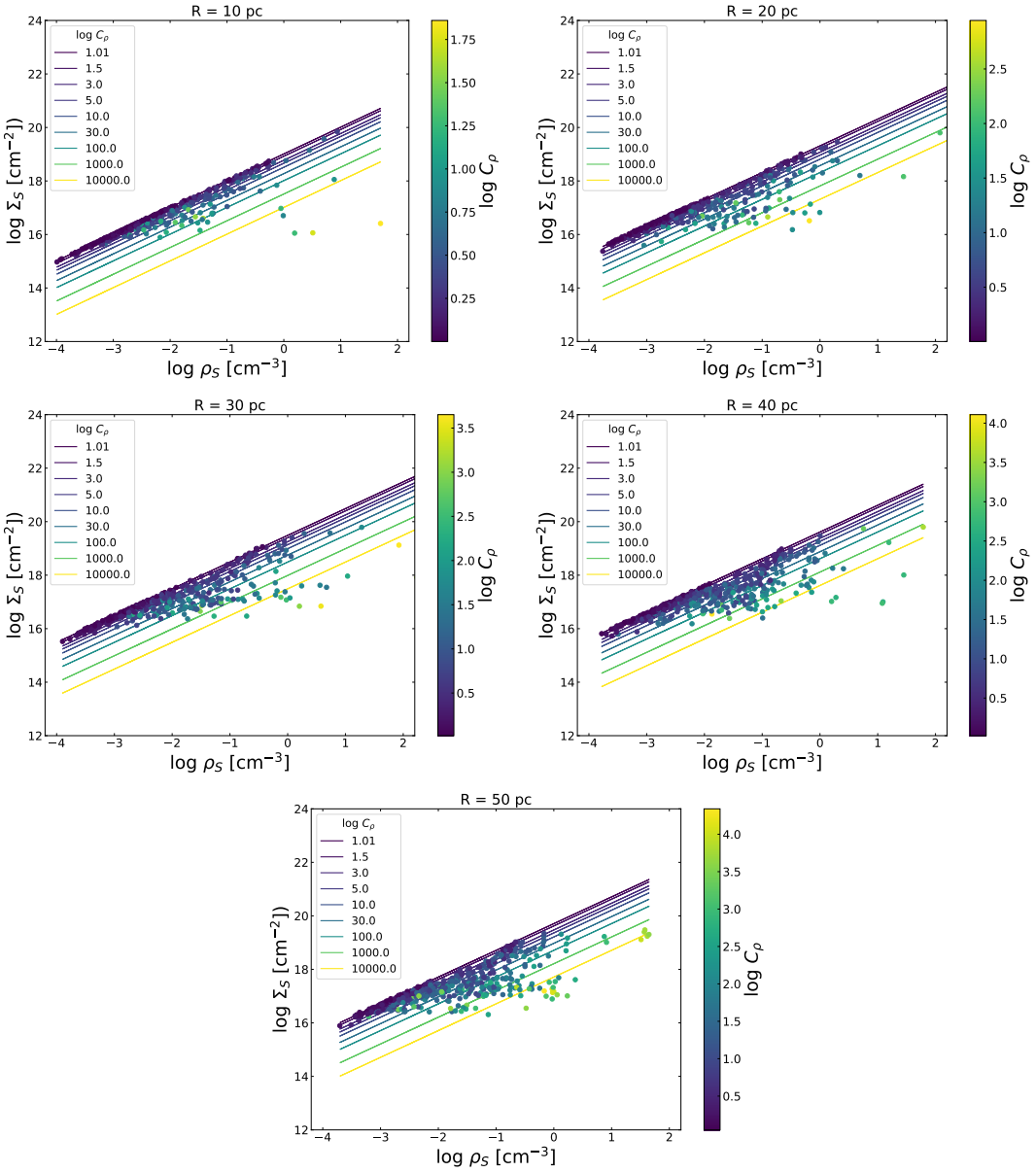

Figure 11: Relation between density and column density for different radii ranging from 10 to 50 pc, with color coding representing the clumping factor for each spheres. The diagonal lines denote the theoretical relation from Equation 21.

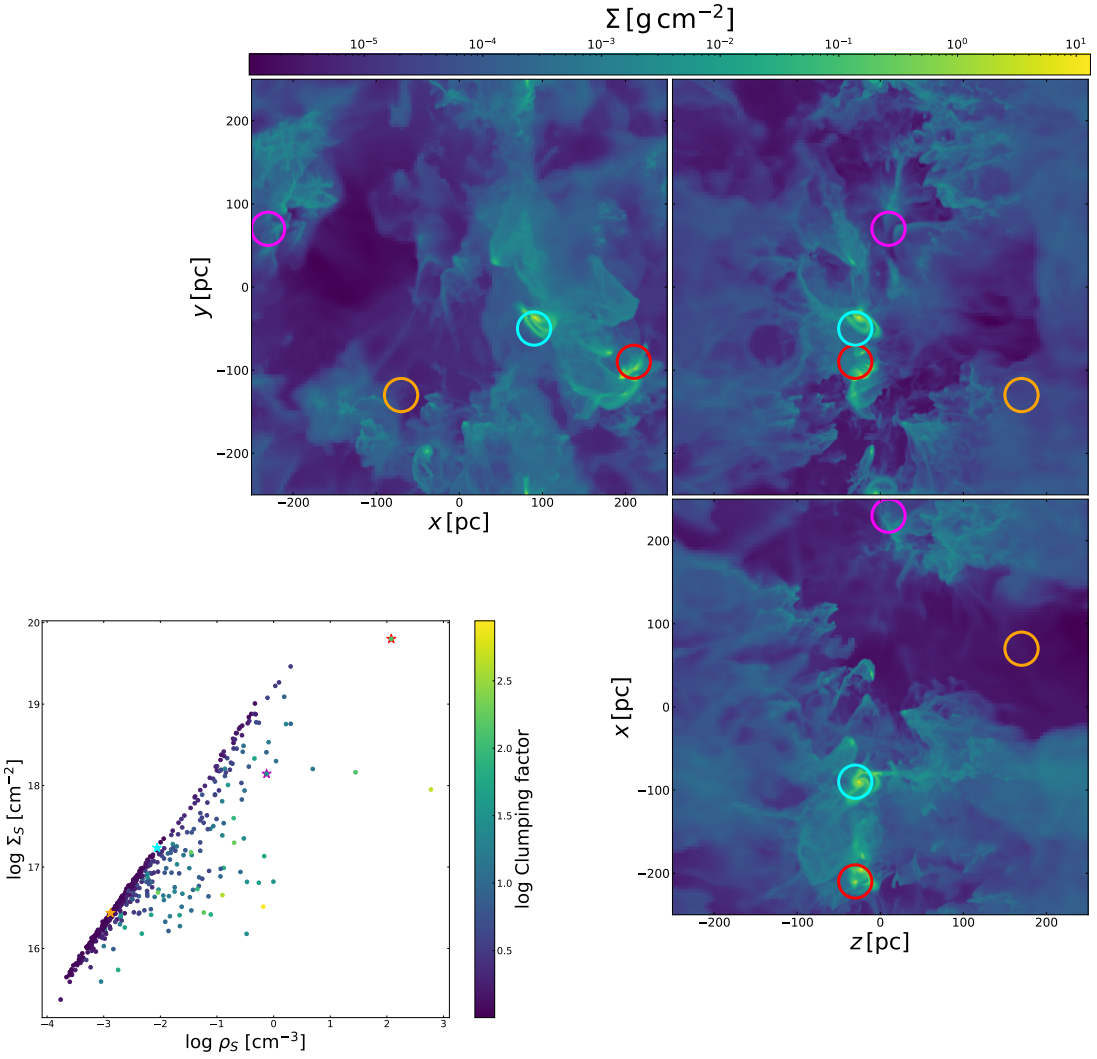

Figure 12: Each point in the bottom-left panel represents a sphere with a radius of 20 pc. The plot shows the relationship between the average density and the median column density for each sphere, with color coding showing the clumping factor. Several points are marked on the plot: those along the linear relation are more uniform regions, while the others represent higher density, clumpy regions. To illustrate this, the locations of the spheres are marked on the other three panels, which show density projections of the snapshot along the three axes.

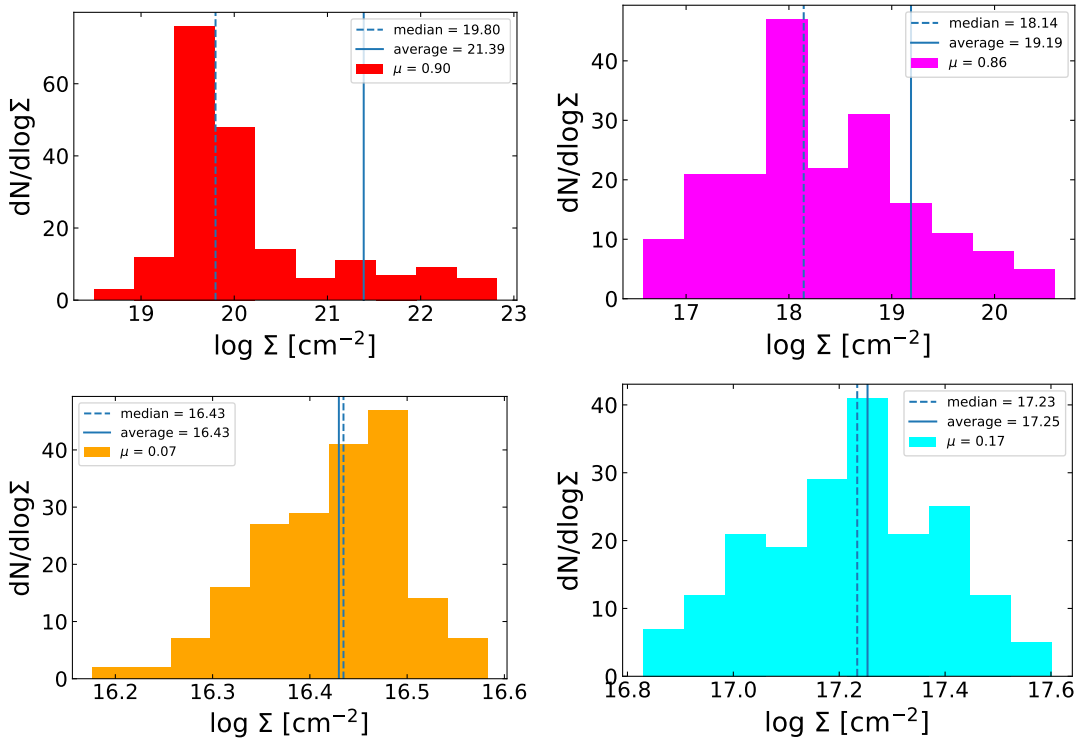

Figure 13: Histograms showing the column density distributions of the spheres highlighted in Figure 12.

density distribution in the ISM is isotropic when averaged over a sufficiently large region, we can consider the density distribution along the three spatial dimensions are independent, as well as normally distributed. Following this argument, we can take the column density Σ distribution, obtained by projecting the three dimensional density distribution f_V along the radial axis, to also be log-normally distributed (this was also verified by analysing the simulation data). The area-weighted LN-PDF of Σ is thus:

$$f_A(\Sigma)d\Sigma = \frac{1}{\sqrt{2\pi}\sigma_\Sigma} \exp\left[-\frac{(\ln\Sigma - \mu_\Sigma)^2}{2\sigma_\Sigma^2}\right]\frac{d\Sigma}{\Sigma} \tag{22}$$

where $\mu_\Sigma = \ln\Sigma_0$ is the characteristic column density and σ_Σ is the width of that distribution.

This can be connected to the covering fraction parameter κ we have introduced in Section 3.2.3 via the cumulative function of the log-normal distribution, which is given by an error function (Elmegreen, 2002; Wada & Norman, 2007). The fraction of lines of sight with column density larger than a threshold $\ln\delta$ is thus given by

$$P(\Sigma \geq \delta) = \frac{1}{2}\left(1 - \mathrm{erf}\left[\frac{\ln(\delta/\Sigma_0)}{\sqrt{2}\sigma_\Sigma}\right]\right) \tag{23}$$

where Σ_0 is the characteristic column density and σ_Σ is the characteristic width of the column density distribution. We introduce a scaled surface density, $\hat{\Sigma}$, a scaled peak position, $\hat{\mu}$, and a scaled width, $\hat{\sigma}$ given by

$$\hat{\Sigma} \equiv \frac{3\delta}{\mathrm{R}\langle\rho\rangle_V}, \qquad \hat{\mu} \equiv -\frac{1}{3}\mathrm{lnC}_\rho, \qquad \hat{\sigma} \equiv \sqrt{\frac{2}{3}\mathrm{lnC}_\rho} \tag{24}$$

Using the assumption that $P(\Sigma \geq \delta) \equiv \kappa$, this becomes

$$\kappa = f(\langle\rho\rangle_V | R, C_\rho, \delta) \tag{25}$$

$$= \frac{1}{2}\left(1 - \mathrm{erf}\left[\frac{\ln\left(\frac{3\delta}{R\langle\rho\rangle_V} C_{\rho^{1/3}}\right)}{\sqrt{2\ln C_\Sigma}}\right]\right) \tag{26}$$

$$= \frac{1}{2}\left(1 - \mathrm{erf}\left[\frac{\ln\hat{\Sigma} - \hat{\mu}}{\sqrt{2}\hat{\sigma}}\right]\right) \tag{27}$$

3.6 Theoretical covering fraction

As a first test for our model, we plot the relation between the average sphere density and covering fraction as described by Equation 23 in Figure 14, for spheres with R = 20 pc and a threshold value of $\delta = 10^{17}\mathrm{cm}^{-2}$.

In a perfectly uniform medium, a plot of the covering fraction as a function of density would resemble a step function: some spheres, with mass distributed in such a way that each channel has a column density below the threshold, have a covering fraction equal to 0, while the other, higher mass spheres will have a covering fraction equal to 1. This case is shown in Figure 14 by the theoretical line corresponding to a clumping factor of 1.01. As the clumping factor in the medium is modified, we find significant and consistent deviations from this basic scenario. By increasing the clumping factor, our model predicts that lower density spheres show higher covering fractions, while higher density spheres show lower covering fractions compared to the most uniform case. This is unsurprising: in a low density sphere (which would not have any line of sight with a column density higher than the threshold if the gas contained within it were distributed evenly) the gas can clump up in some regions, creating a number of lines of sight with column density above the threshold. The same process will have the opposite happens in high density regions. While evenly distributing the gas in such a sphere would mean every line of sight has a column density above the threshold, clumping can

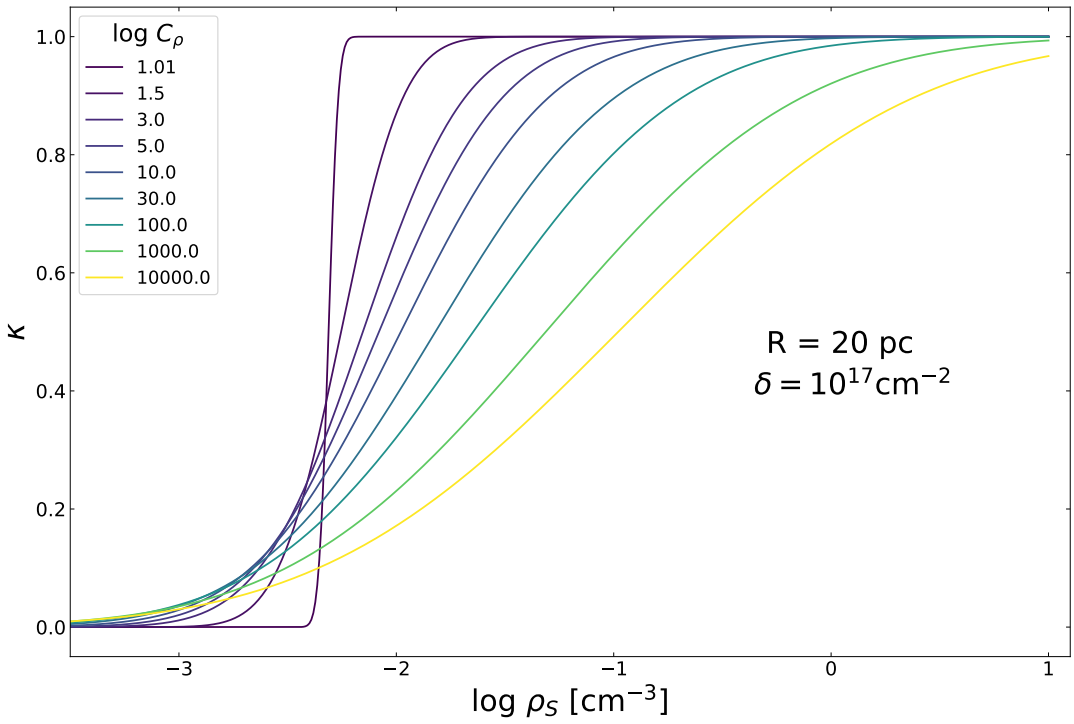

Figure 14: Theoretical relation between density and covering fraction for spheres with R = 20 pc and a column density threshold of $\delta = 10^{17}\mathrm{cm}^{-2}$. Color coding illustrates this relation, as described by Equation 27, for different values of the clumping factor.

take gas away from some channels, leaving them underdense compared to that reference value.

In order to verify the validity of this model, we compare its predictions to some of the results obtained from the SILCC simulation, in particular looking at the relation between sphere density and covering fraction. We start by checking what is the effect of modifying the threshold value used to compute the covering fraction. It is reasonable to expect that, with a lower threshold, more spheres will be characterized by a higher covering fraction parameter (the opposite being true for a higher threshold). This is illustrated by Figure 15.

Another scenario we examine is one in which the sphere radii are increased from 10 pc to 50 pc (representing a reasonable set of scales for gas structures in the ISM), as seen in Figure 16. In this case, we note a pattern where an "upturn" in the density to covering fraction relation appears to shift as the sphere radius increases. This upturn roughly corresponds to the density at which spheres are found to have values of the covering fraction that are close to 1. For larger spheres,

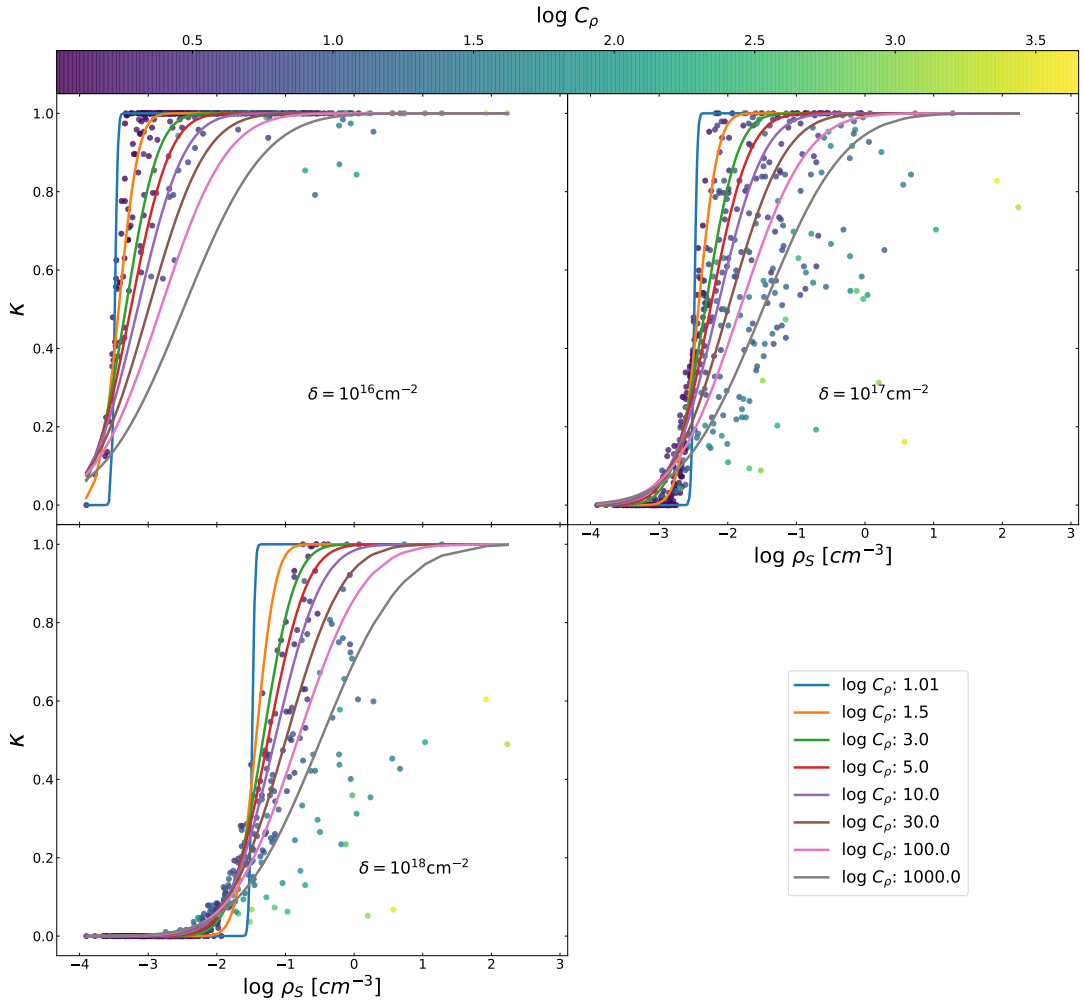

Figure 15: Relation between density and covering fraction for different values of the column density threshold, with color coding denoting the clumping factor in each sphere. The theoretical relation between these parameters, as described by Equation 27, is overplotted for a series of values of the clumping factor.

this happens at lower average densities than in the case of smaller spheres. This is expected due to the fact that their radii are larger and thus we are integrating over a larger number of gas particles.

Our analysis shows that larger spheres tend to be characterized by higher clumping factors. This is due to fact that, within a larger volume, it is possible to find more regions with large differences in density between them. Quantitatively, this is illustrated in Table 3, which shows the clumping factor distribution as a function of density and sphere radius.

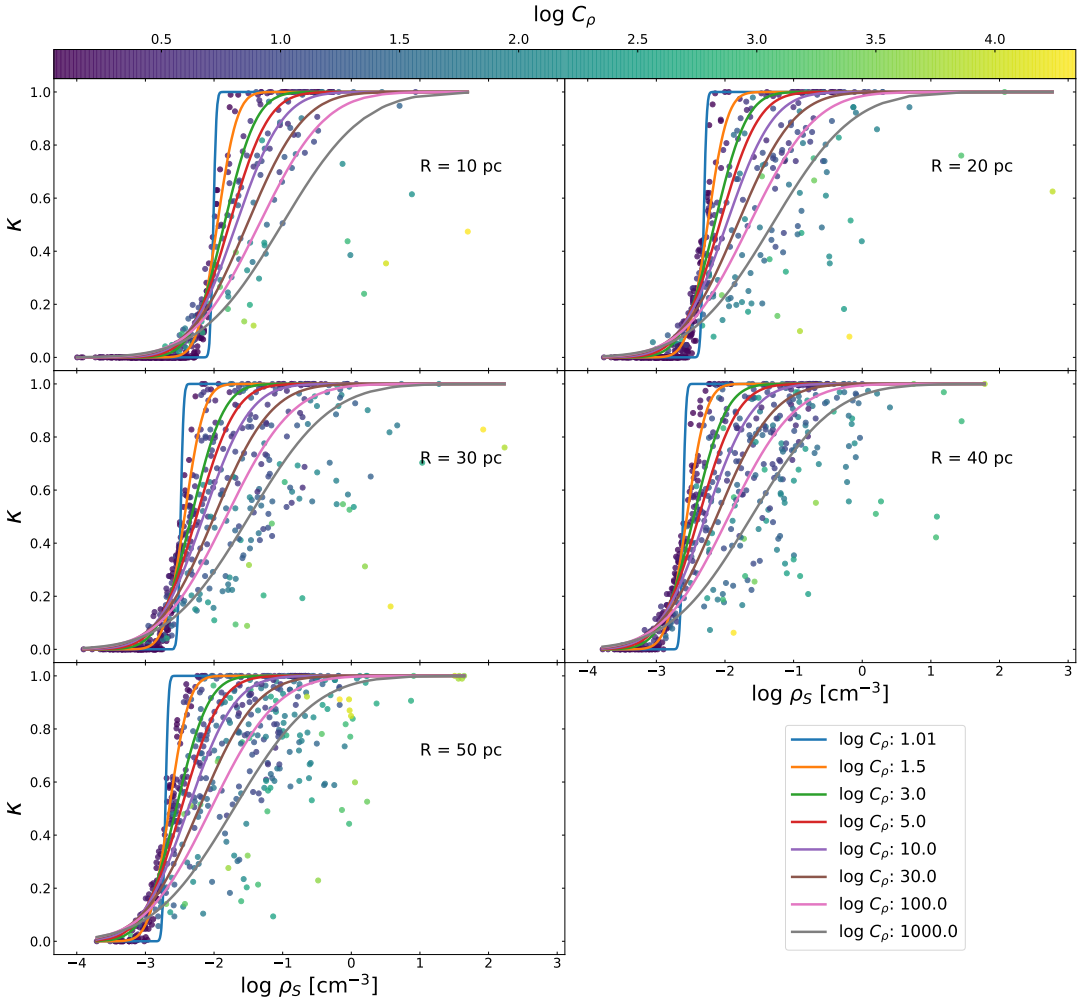

Figure 16: Relation between density and covering fraction using spheres of different radii. Once again we overplot the theoretical relation between these parameters, as described by Equation 27, for different values of the clumping factor. The increase in radius shifts the distribution towards lower average densities, i.e. the observed increase in covering fraction occurs for spheres with a *lower* average density.

Table 3: Clumping factor distributions as a function of density and sphere radius as derived from the SILCC simulations. For each radius we state the median, 32^{nd} and the 68^{th} percentile of the clumping factor for a range of 1 dex wide ISM density bins.

R [pc]	$\log_{10}\left(\frac{\rho}{\text{cm}^{-3}}\right)$				
	$(-4,-3)$	$(-3,-2)$	$(-2,-1)$	$(-1,0)$	$(0,1)$
10	$0.02^{0.05}_{0.01}$	$0.05^{0.12}_{0.02}$	$0.54^{1.08}_{0.2}$	$0.19^{0.97}_{0.09}$	$1.79^{2.22}_{1.39}$
20	$0.08^{0.13}_{0.03}$	$0.14^{0.27}_{0.06}$	$1.39^{2.09}_{0.87}$	$1.17^{2.12}_{0.52}$	$3.76^{4.66}_{2.66}$
30	$0.14^{0.2}_{0.08}$	$0.26^{0.48}_{0.16}$	$1.58^{2.14}_{1.04}$	$1.89^{3.42}_{1.14}$	$3.07^{4.15}_{2.79}$
40	$0.15^{0.26}_{0.11}$	$0.42^{0.75}_{0.26}$	$2.08^{2.75}_{1.71}$	$2.34^{3.59}_{1.98}$	$5.32^{5.49}_{5.2}$
50	$0.17^{0.29}_{0.13}$	$0.55^{0.82}_{0.33}$	$2.36^{2.76}_{1.86}$	$3.03^{4.02}_{2.2}$	$5.87^{6.15}_{5.43}$

3.7 Stellar wind modelling

Stars form from the fragmentation and collapse of giant cold gas clouds in the galaxy. From the beginning of their lifetime to the end, stars in turn influence the ISM through a series of feedback processes: protostellar outflows, radiation, stellar winds, and supernovae (Girichidis et al., 2020). The latter two are the most important and become significant particularly for high mass stars.

For the second part of our analysis we model the mass loss and kinetic energy output of massive stars with a wide range of stellar masses. The goal is to develop a model which can be implemented in hydrodynamical simulations and investigate the effects of feedback from stellar winds throughout the lifetime of a massive star in comparison to that of supernova explosions. One potential application for this work is to obtain cosmic ray (CR) maps for CRs accelerated at stellar wind terminal shocks.

3.7.1 Methods

We use the stellar evolution tracks computed by Ekström et al. (2012) and Georgy et al. (2012). Data is available for stars with masses ranging from 0.8 to 120 $M_\odot$, at solar metallicity Z = 0.014, with and without rotation. For our analysis we use the models with rotation for the most massive stars, i.e. for 7, 9, 12, 15, 20, 25, 32, 40, 60, 85, and 120 $M_\odot$, since only starting with these masses does the mass loss via stellar winds become important for the ISM.

The parameters used to define stellar winds are the mass loss rate, $\dot{M}$, and the terminal wind velocity, v_{wind}. The former can be obtained directly from the stellar evolution tracks, while for the latter we must perform some intermediate steps. We first split the model tracks into their evolutionary phases, following

Stellar mass ($M_\odot$)	A	n	b
7	0.68090928	3.08182208	43.63162516
9	1.1465175	3.96926923	44.77376765
12	1.44313612	4.29800498	45.71879725
15	1.72165227	4.81014221	46.15744546
20	2.73580642	6.90966359	45.62681469
25	2.70257286	6.60933616	46.18721233
32	2.3860646	5.61960684	47.0047701
40	2.30189756	5.1658291	47.48097047
60	3.	6.06627166	47.37047923
85	3.	6.39558796	47.78034142
120	3.	6.40195934	48.112979

Table 4: Wind luminosity fit parameters for massive stars.

a procedure outlined in Gatto et al. (2016). According to effective temperature and H mass fraction we classified stars as WR stars, WC stars, or O-type stars. We then compute terminal wind velocities for the different evolutionary phases via linear interpolation and plot this data in Figure 17.

3.7.2 Results

In order to obtain a model that is more useful for our purpose, we use the *cumulative* mass loss and wind luminosity, which can be fit using simple continuous or piecewise continuous functions. The resulting profiles are shown in Figure 18.

We found that the best fit in both cases is a "stretched" square root function of the form

$$A \cdot x^{1/n} + b \tag{28}$$

After performing a least-squares fit for the different profiles, a different set of A, n, and b parameters were obtained for each of the eleven model tracks available.

For the wind luminosity, the parameters are collected in Table 4. Energy loss can be modelled using a continuous function, so a single set of values was determined for every stellar mass. The cumulative mass loss parameters are collected in Table 5. For most massive stars, towards the end of their lifetime, there is a significant increase in mass loss after the point when helium burning begins in the core (Ekström et al., 2012). This means that two sets of parameters are needed to fully model mass loss, one for the stellar evolution stage before helium ignition and the other for the stage after helium burning begins.

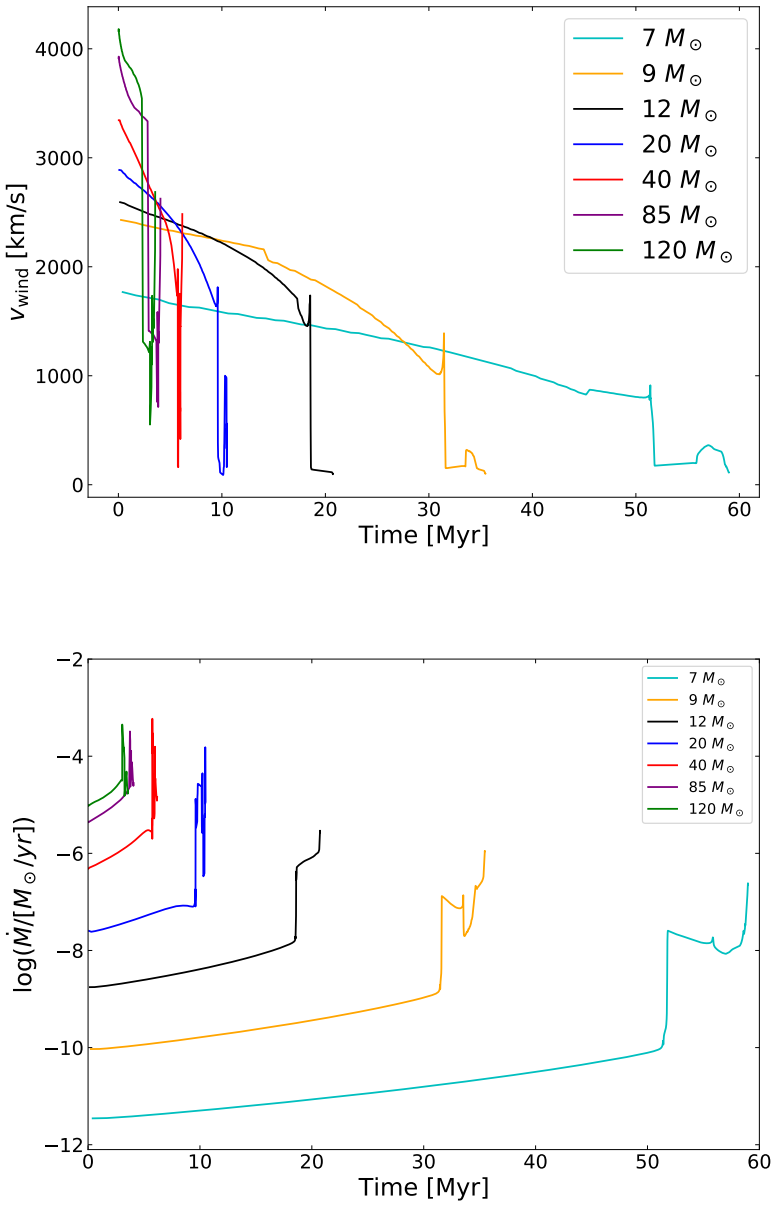

Figure 17: Terminal wind velocities (*above*) and mass loss (*below*) for a sample of stellar masses for which stellar evolution tracks are available.

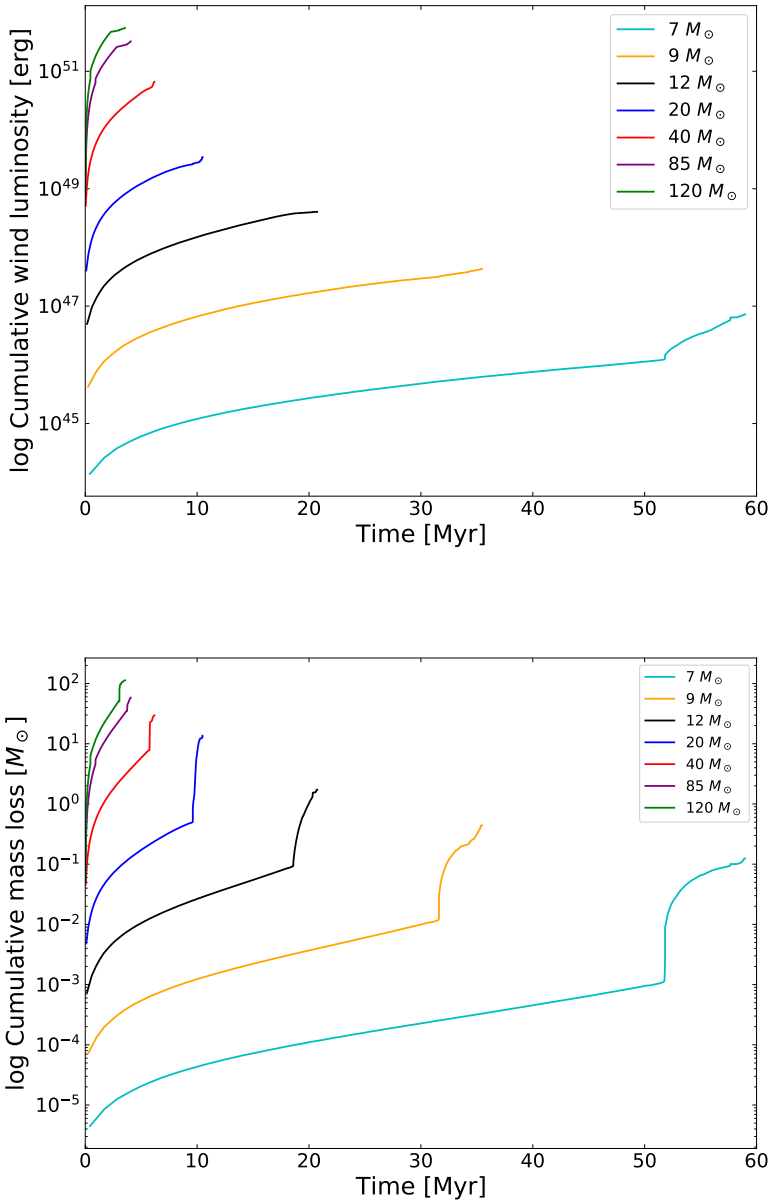

Figure 18: Cumulative wind luminosity (*above*) and cumulative mass loss (*below*). The upturn in mass loss occurs after helium burning begins in the stellar core.

Stellar mass ($M_\odot$)	A	n	b
7	0.18959081	1.57738276	-5.25303223
9	0.41127795	2.0037655	-4.23440433
12	0.75445111	2.53992044	-3.42615701
15	0.93307792	2.75208386	-2.94271089
20	1.46560372	3.59955226	-3.0448446
25	1.5172324	3.47789122	-2.60948064
32	1.46410675	3.15198665	-2.09379407
40	1.49249924	3.01621589	-1.76034773
60	3.38726058	5.79783191	-3.06870642
85	6.76436573	11.88215787	-6.01680174
120	6.52683199	10.28156331	-5.35482247

Stellar mass ($M_\odot$)	A	n	b
7	0.42879364	2.50367269	-1.86195141
9	0.34960683	1.47185531	-1.25156138
12	0.91043414	2.11146345	-1.0585865
15	1.00751871	1.81845407	-0.60985222
20	1.62268526	2.92180534	-0.31750544
25	0.90949382	6.56591282	0.34365337
32	0.56140679	4.02673117	0.88819976
40	0.36691989	1.3528952	1.28029779
60	0.34061041	1.93021728	1.45082884
85	0.33583966	1.48857532	1.61358175
120	0.11649451	1.23411731	2.00537784

Table 5: Cumulative mass loss fit parameters for massive stars. Mass loss is modelled using two different sets of parameters for the two different stages of stellar evolution relevant for this analysis: before (*top*) and after (*bottom*) helium burning starts in the core.

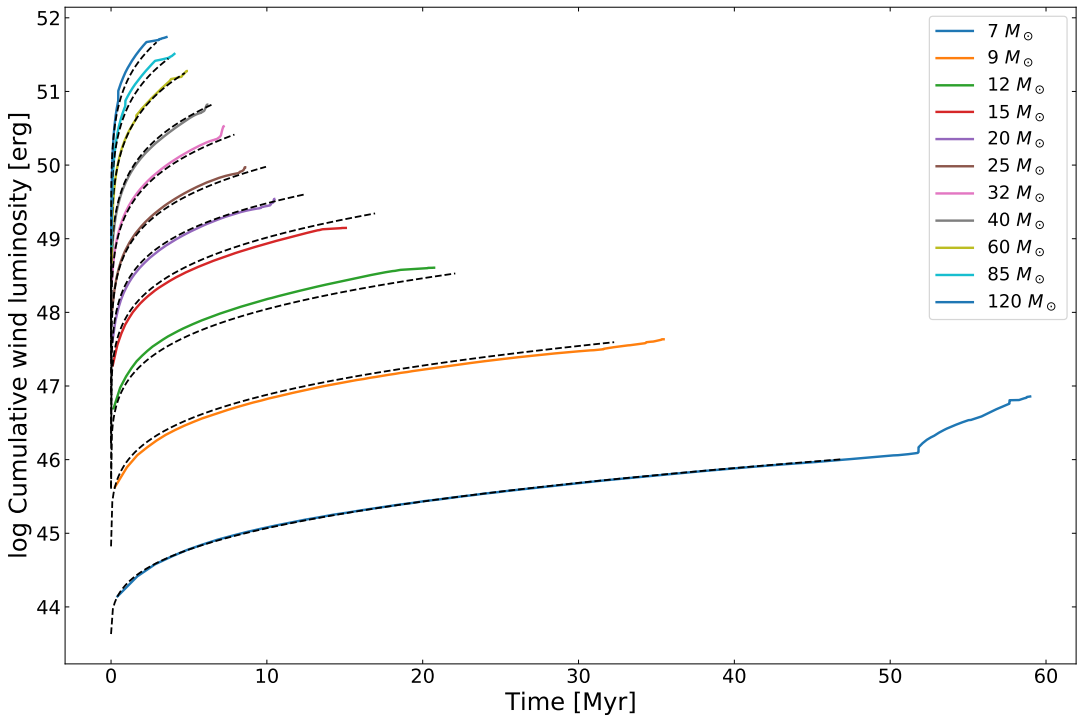

Figure 19: Cumulative wind luminosities for different stellar masses (full lines, color coding denotes mass) compared to profiles obtained from Equation 28 after recovering the fit parameters from a secondary fitting process (dashed lines). While errors are to be expected from such a process, the results are not entirely unreasonable, especially given the inherent uncertainties in stellar wind modelling.

In order to obtain tracks for the intermediate stellar mass values, we also attempt to fit this newly obtained set of parameters with piecewise linear functions (in log space). While this approach works in principle, the double fitting process will unavoidably propagate errors. This becomes clear when attempting to recover the initial stellar evolution tracks by first *computing* the values of the A, n, and b parameters from the secondary fit (*instead* of using the tabulated values) and recreating the track by plotting Equation 28 with them.

In addition to these fitting function parameters, another function is needed to determine the maximum age for every stellar mass. Finally, the point during the lifetime of a star when helium burning begins also needs to be obtained, also by fitting the stellar tracks.

To illustrate this, the results for the cumulative wind luminosity are shown in Figure 19. While the recovered functions do not coincide with the initial

tracks, they are not entirely unreasonable. Stellar mass loss is still not a fully understood process (Renzo et al., 2017), so any model will have an inherent degree of uncertainty.

Developing a simple, empirical model for stellar winds would be very useful for implementing stellar winds with numerical codes. Obtaining the mass loss within a given timestep can be easily done by computing the difference in cumulative mass loss between two points separated by that time interval. While the method presented in this work certainly needs to be improved, such an approach is preferable to obtaining the results by running a stellar evolution code (e.g. MESA, Paxton et al., 2011), which can be cumbersome, in particular if the project is on the scale of a galaxy simulation.

4 Discussion and Summary

Here we provide a summary of the ISM density structure model and briefly mention some potential applications, caveats, and avenues for future research, following Buck et al., submitted to MNRAS, under review.

4.1 Applications and outlook

The analysis presented in this work evolved from an initial goal of modelling a star injecting energy and momentum into the surrounding gas. The stellar wind model could be implemented with numerical codes in order to simulate the effects young massive stars have on their environment. As we mentioned in Section 2.8.2, CRs can be accelerated at stellar wind shocks. Therefore, by approximating the number of massive stars (using an appropriate integrated galactic initial mass function, see Kroupa & Weidner, 2003) and modelling their output, it would be possible to estimate the contribution massive stars have on galactic CR acceleration.

Another potential application of this model is estimating the amount of radiation which can escape from a molecular cloud where a star has formed. Since it is to be expected that photons escape more easily through low density regions, the covering fraction can essentially be used as a proxy for optical thickness. Not only radiation, but also momentum injection from stellar winds and supernova explosions are affected by the gas structure. The evolution of a supernova remnant is dependent on the efficiency with which energy from the supernova explosion is transferred to the surrounding gas. This efficiency depends on the density and the density distribution of the medium, as well as the turbulent Mach number $\mathcal{M}$ (see, e.g., Haid et al., 2016). A better model of the gas structure at a given density could potentially improve momentum injection schemes.

4.2 Caveats

One potential limitation of this model comes from the assumption that the ISM gas density follows a log-normal distribution. This assumption is no longer valid at the point where self-gravity becomes important, i.e. at the higher end of the density distribution (see Section 2.5). However it is possible to use a similar method to re-derive the equations for a different density PDF without changing the model.

In addition to this, we computed the clumping factor based only on the density properties of the simulation cells. Different methods of determining this parameter can be used, which explicitly take into account additional physics (e.g.

Equation 7, where the clumping factor is a function of the turbulence driving parameter and the Mach number).

4.3 Summary of the ISM gas density model

The ISM gas structure statistical model presented in this work can be summarized thus:

- Assuming that the ISM density distribution has the shape of a log-normal, we define a gas (volume) density clumping factor, C_ρ. The relation between C_ρ and the projected clumping factor is given by Equation 20.
- We defined the covering fraction as the number of sight lines with column density above a preset threshold column density to the total number of sight lines. In this analysis the total number of sight lines corresponds to the number of HEALPix pixels which fully cover the surface of imaginary spheres randomly sampled from the simulation box. We find that the relation between the volume density of these spheres and the covering fraction can be described by an error function (which is the cumulative of a log-normal PDF). The peak and width of the density distribution for each sphere can be determined from the column density threshold, the radius of the spheres, and the clumping factor, the latter being the only free parameter in this model.
- There is a relation between average density and clumping factor in the ISM. For every density and sphere radius there is a range of reasonable values of the clumping factor which can be sampled (see Table 3). We computed these values using data from the SILCC simulation.
- The clumping factor can be used to determine the covering fraction at the relevant density. We have found that, at a given density, the covering fraction in regions of different sizes can vary significantly. Setting a reasonable value for the clumping factor, the covering fraction ca be obtained using Equation 27. With the appropriate model (e.g., what is the column density threshold at which a cloud becomes optically thick) it is straightforward to estimate the density structure of the ISM on scales of ~ 10 pc. This can subsequently be used to infer photon escape fractions or model energy and momentum injection into the ISM gas.

5 Conclusion

We set out to provide a description of the density structure of the ISM. We start with an accounting of the average density and average column density and the relation between them. The columns in our case are lines of sight having one end in the center of the sphere and the other corresponding to a HEALPix pixel on its surface.

Both ρ and Σ_a decrease with simulation time, even without sinks or mass loss processes. This can be explained by structure formation: as the simulation evolves, gas clumps up and becomes less uniform. After such structures form, it is more likely that we sample spheres from voids than from overdense regions, leading to this observed trend.

Such an evolution in density is also apparent in the relationship between average density and column density width ω_{16}^{84}. At later times in the simulation we find more low density, low column density width spheres, suggesting that more of the space is filled with less dense, more uniform regions. Higher density spheres are also characterized by a higher ω_{16}^{84} parameter, as well as a higher clumping factor, which suggests regions containing denser gas are also more structured. This is a reasonable expectation and is consistent with our picture of structure formation: a fraction of the gas tends to clump up into dense, non-uniform subclouds, while the leftover gas, which fills most of the rest of space, remains as a more tenuous and more uniform medium.

We have defined the covering fraction as the fraction of lines of sight within a sphere which have a column density that is higher than a chosen threshold value. We found that within a particular range of threshold values, between 10^{17} and 10^{19} cm^{-2}, we obtain results that are useful for developing density structure model. Outside of this range, virtually all spheres are either completely optically thin, or completely optically thick. Within this range of threshold values, we found that the relation between average sphere density and covering fraction can be represented by an error function, which is the cumulative of a log-normal PDF, as expected for the log-normal gas density distribution of the ISM.

Finally, we have defined a clumping factor and found that there is a range of reasonable values that this parameter can have at a given density and spatial scale of the ISM region. The clumping factor can be used to model the scatter in the covering fraction to density relation.

I hereby confirm that solely I am the author of this thesis and have not used other sources and resources than the ones cited. The thesis on hand is free of plagiarisms. All information that has been extracted directly or indirectly from other works is marked as such and listed in the table of references. This work has not been handed in as an assessed assignment with another examiner and has not been published before.

I have been informed that a plagiarism detection software will be used in order to check my thesis for its legitimacy. I am aware that my anonymized thesis will be analyzed in a secure domain of a server outside of the European Union and is temporarily saved there. For this, no personal data will be transmitted. I hereby consent to the checking of my thesis through a plagiarism detection software under the before mentioned conditions.

December 14, 2021 Bogdan-Vasile Corobean

References

Axford W. I., Leer E., Skadron G., 1977, in International Cosmic Ray Conference. p. 132

Balbus S. A., Hawley J. F., 1991, ApJ, 376, 214

Ballesteros-Paredes J., Vázquez-Semadeni E., Gazol A., Hartmann L. W., Heitsch F., Colín P., 2011, MNRAS, 416, 1436

Belczynski K., et al., 2020, ApJ, 890, 113

Bell A. R., 1978a, MNRAS, 182, 147

Bell A. R., 1978b, MNRAS, 182, 443

Bialy S., Sternberg A., 2019, ApJ, 881, 160

Bigiel F., Leroy A., Walter F., Brinks E., de Blok W. J. G., Madore B., Thornley M. D., 2008, AJ, 136, 2846

Bigiel F., et al., 2011, ApJ, 730, L13

Blandford R. D., Ostriker J. P., 1978, ApJ, 221, L29

Blasi P., 2013, A&A Rev., 21, 70

Bonnell I. A., Bate M. R., Clarke C. J., Pringle J. E., 2001, MNRAS, 323, 785

Castor J. I., Abbott D. C., Klein R. I., 1975, ApJ, 195, 157

Crowther P. A., 2007, ARA&A, 45, 177

Draine B. T., 2003, ARA&A, 41, 241

Drury L. O., 1983, Reports on Progress in Physics, 46, 973

Ekström S., et al., 2012, Astronomy & Astrophysics, 537, A146

Elmegreen B. G., 2002, ApJ, 577, 206

Elmegreen B. G., Burkert A., 2010, ApJ, 712, 294

Falceta-Gonçalves D., Kowal G., Falgarone E., Chian A. C. L., 2014, Nonlinear Processes in Geophysics, 21, 587

Federrath C., Klessen R. S., 2012, ApJ, 761, 156

Federrath C., Klessen R. S., Schmidt W., 2008, http://dx.doi.org/10.1086/595280 ApJ, 688, L79

Federrath C., Roman-Duval J., Klessen R. S., Schmidt W., Mac Low M. M., 2010, A&A, 512, A81

Fermi E., 1949, Physical Review, 75, 1169

Field G. B., Goldsmith D. W., Habing H. J., 1969, ApJ, 155, L149

Gatto A., et al., 2016, Monthly Notices of the Royal Astronomical Society, 466, 1903–1924

Georgy C., Ekström S., Meynet G., Massey P., Levesque E. M., Hirschi R., Eggenberger P., Maeder A., 2012, http://dx.doi.org/10.1051/0004-6361/201118340 A&A, 542, A29

Girichidis P., et al., 2016, Monthly Notices of the Royal Astronomical Society, 456, 3432–3455

Girichidis P., et al., 2020, Space Science Reviews, 216

Glover S. C. O., Clark P. C., 2014, MNRAS, 437, 9

Gnedin N. Y., Tassis K., Kravtsov A. V., 2009, ApJ, 697, 55

Gorski K. M., Hivon E., Banday A. J., Wandelt B. D., Hansen F. K., Reinecke M., Bartelmann M., 2005, The Astrophysical Journal, 622, 759–771

Gould R. J., Salpeter E. E., 1963, ApJ, 138, 393

Haffner L. M., et al., 2009, Reviews of Modern Physics, 81, 969

Haid S., Walch S., Naab T., Seifried D., Mackey J., Gatto A., 2016, MNRAS, 460, 2962

Heiles C., Troland T. H., 2003, ApJ, 586, 1067

Hellwig H., Vessot R. F. C., Levine M. W., Zitzewitz P. W., Allan D. W., Glaze D. J., 1970, IEEE Transactions on Instrumentation and Measurement, 19, 200

Heyer M. H., Brunt C. M., 2004, ApJ, 615, L45

Heyer M., Krawczyk C., Duval J., Jackson J. M., 2009, ApJ, 699, 1092

Hillas A. M., 1984, ARA&A, 22, 425

Hoyle F., 1946, MNRAS, 106, 384

Hoyle F., Ellis G. R. A., 1963, Australian Journal of Physics, 16, 1

Jeans J. H., 1902, Philosophical Transactions of the Royal Society of London Series A, 199, 1

Jura M., 1975, ApJ, 197, 575

Kainulainen J., Beuther H., Henning T., Plume R., 2009, A&A, 508, L35

Kennicutt Robert C. J., 1998, ApJ, 498, 541

Kennicutt R. C., Evans N. J., 2012, ARA&A, 50, 531

Klessen R. S., Glover S. C. O., 2014, Physical Processes in the Interstellar Medium (http://arxiv.org/abs/1412.5182 `arXiv:1412.5182`)

Klessen R. S., Hennebelle P., 2010, A&A, 520, A17

Kroupa P., Weidner C., 2003, ApJ, 598, 1076

Krumholz M. R., 2015, arXiv e-prints, p. arXiv:1511.03457

Krumholz M. R., Bonnell I. A., 2007, arXiv e-prints, p. arXiv:0712.0828

Krumholz M. R., Burkhart B., 2016, MNRAS, 458, 1671

Krumholz M. R., Tan J. C., 2007, ApJ, 654, 304

Krymskii G. F., 1977, Akademiia Nauk SSSR Doklady, 234, 1306

Larson R. B., 1981, MNRAS, 194, 809

Larson R. B., 2003, Reports on Progress in Physics, 66, 1651

Leroy A. K., Walter F., Brinks E., Bigiel F., de Blok W. J. G., Madore B., Thornley M. D., 2008, AJ, 136, 2782

Licquia T. C., Newman J. A., 2015, ApJ, 806, 96

McKee C. F., Ostriker J. P., 1977, ApJ, 218, 148

McKee C. F., Ostriker E. C., 2007, ARA&A, 45, 565

Miville-Deschênes M.-A., Murray N., Lee E. J., 2017, ApJ, 834, 57

Muijres L. E., 2010, PhD thesis, University of Amsterdam

Owocki S. P., Cohen D. H., 2006, http://dx.doi.org/10.1086/505698 ApJ, 648, 565

Parker E. N., 1958, ApJ, 128, 664

Parker E. N., 1960, ApJ, 132, 821

Paxton B., Bildsten L., Dotter A., Herwig F., Lesaffre P., Timmes F., 2011, ApJS, 192, 3

Pillepich A., et al., 2018, MNRAS, 473, 4077

Puls J., Vink J. S., Najarro F., 2008, A&A Rev., 16, 209

Renzo M., Ott C. D., Shore S. N., de Mink S. E., 2017, A&A, 603, A118

Robitaille T. P., Whitney B. A., 2010, ApJ, 710, L11

Roman-Duval J., Jackson J. M., Heyer M., Rathborne J., Simon R., 2010, ApJ, 723, 492

Schaye J., et al., 2015, MNRAS, 446, 521

Schmidt M., 1959, ApJ, 129, 243

Seo J., Kang H., Ryu D., 2018, Journal of Korean Astronomical Society, 51, 37

Solomon P. M., Rivolo A. R., Barrett J., Yahil A., 1987, ApJ, 319, 730

Tan J. C., Beltrán M. T., Caselli P., Fontani F., Fuente A., Krumholz M. R., McKee C. F., Stolte A., 2014, in Beuther H., Klessen R. S., Dullemond C. P., Henning T., eds, Protostars and Planets VI. p. 149

Tremmel M., et al., 2019, http://dx.doi.org/10.1093/mnras/sty3336 MNRAS, 483, 3336

Trumpler R. J., 1930, PASP, 42, 214

Urošević D., Arbutina B., Onić D., 2019, Ap&SS, 364, 185

Vazquez-Semadeni E., 1994, ApJ, 423, 681

Wada K., Norman C. A., 2007, ApJ, 660, 276

Walch S., et al., 2015, Monthly Notices of the Royal Astronomical Society, 454, 246–276

Weaver R., McCray R., Castor J., Shapiro P., Moore R., 1977, ApJ, 218, 377

Webb G. M., Axford W. I., Forman M. A., 1985, ApJ, 298, 684

Widrow L. M., 2002, Reviews of Modern Physics, 74, 775

Wiersma R. P. C., Schaye J., Smith B. D., 2009, MNRAS, 393, 99

Williams D. A., 2005, in Journal of Physics Conference Series. pp 1–17

Williams J. P., McKee C. F., 1997, ApJ, 476, 166

Wolfire M. G., McKee C. F., Hollenbach D., Tielens A. G. G. M., 2003, ApJ, 587, 278

van Dishoeck E. F., Black J. H., 1986, ApJS, 62, 109